Hollow Core Plasma Channel Generation

Heinrich Martin Quast

MASTERARBEIT

eingereicht am
Masterstudiengang

Physik

Universität Hamburg

im Dezember 2017

Gutachter
1. Dr. Jens Osterhoff
2. Prof. Brian Foster

Abstract

The use of a hollow plasma channel in plasma-based acceleration has beneficial properties for the acceleration of electron and positron bunches. In the scope of the FLASHForward facility at DESY, the generation of such a plasma structure is examined. Therefore, the generation of a ring-shaped laser intensity profile with different techniques is analyzed.

From the obtained intensity profiles the electron density of a hollow plasma channel is simulated in the focal region. Different parameters are scanned to understand their influence on the electron density distribution - an important parameter being, for example, the radius of the central region of the channel.

In addition to the simulations, experiments are presented, during which a laser pulse is transformed into a hollow beam with a spiral phase plate. Subsequently, it forms a plasma during the interaction with hydrogen, where the plasma is imaged with interferometry. For energies above $0.9\,\mathrm{mJ}$ a hollow plasma structure can be observed at the location of first plasma formation.

Kurzfassung

Die Verwendung eines hohlen Plasmakanals bei der plasmabasierten Beschleunigung hat vorteilhafte Eigenschaften für die Beschleunigung von Elektronen- und Positronenbündeln. Im Rahmen der FLASHForward-Anlage bei DESY wird die Entstehung einer solchen Plasmastruktur untersucht. Es wird die Erzeugung eines ringförmigen Laserintensitätsprofils mit verschiedenen Techniken analysiert.

Aus den erhaltenen Intensitätsprofilen wird die Elektronendichte eines hohlen Plasmakanals im Fokusbereich simuliert. Verschiedene Parameter werden gescannt, um ihren Einfluss auf die Elektronendichteverteilung zu verstehen - ein wichtiger Parameter ist zum Beispiel der Radius des zentralen Bereichs des Kanals.

Neben den Simulationen werden Experimente vorgestellt, bei denen ein Laserpuls mit einer Spiralphasenplatte in einen Hohlstrahl umgewandelt wird. Anschließend bildet dieser bei der Wechselwirkung mit Wasserstoff ein Plasma, wobei das Plasma interferometrisch abgebildet wird. Für Energien über 0.9 mJ kann eine hohle Plasmastruktur am Ort der ersten Plasmabildung beobachtet werden.

Contents

Chapter 1

Introduction

Electron beams with high energies find application in several scientific fields such as a source for free-electron laser (FEL), for example the X-FEL at Deutsches Elektronen-Synchrotron (DESY), in material and life science or in colliders for particle physics. At the Large Hadron Collider at CERN, for example, the Higgs-boson was discovered at a center of mass energy of $E \approx 7\,\mathrm{TeV}$ [1]. Reaching these energies with conventional radio frequency accelerators requires distances on the kilometer scale because these are limited to acceleration gradients around $50\,\mathrm{MV/m}$ [2] due to material breakdown.

To overcome this limit in accelerating gradient other possible methods for the acceleration of particles are being investigated. In 1979 Tajima and Dawson [3] proposed to use the electric fields generated by the charge separation in a plasma for the use in electron acceleration. These electric fields can be created with a high-intensity laser pulse. It was only at that time, that laser systems were powerful enough to provide sufficient energies to the plasma to drive a plasma wave. This method has proven very effective since, mainly because gradients in the GV/m range are achievable - three orders of magnitude higher than before([4],[5]). The accelerator becomes very compact, as the accelerating distance is only a few cm long[6].

The FLASHForward facility[7] is a plasma-based accelerator beamline at the free-electron laser FLASH at the DESY. The primary goal of this experiment is to demonstrate acceleration of electron beams with sufficient quality to be able to achieve FEL gain. FLASHForward does not use a laser to drive a wakefield but instead uses an electron beam for the acceleration. However, since the field of the electron beam is not strong enough to ionize the hydrogen gas in the interaction region, the plasma is created by a 25 TW laser system. The plasma wave is then driven by an electron bunch from the FLASH linear accelerator. In the excited waves, an injected witness bunch may then be accelerated to GeV energies.

In those wakefields not only accelerating longitudinal electric fields exist, but beams also feel strong transverse forces that can limit beam quality. Not matching the injected beam to the plasma waves can lead to emittance growth[8]. Hollow plasma channels have been proposed to tackle this problem. The transverse shape of these channels allows for the independent control over accelerating and focusing fields. Furthermore, this structure can be used for beams of either charge. The acceleration of positrons in the non-linear regime is challenging in the wakefield produced with a uniform plasma. The region in which the wakefields are both accelerating and focusing is located at the back of the wakefield, where the plasma electrons meet on axis. This region is very small compared to the region available for electron acceleration. In this possible location in the wakefield for the positron bunch the plasma electron density is not uniform. This means, that the focusing force and the accelerating gradient vary transversely([8],[9]).

The goal of this thesis is the generation and characterization of a hollow core plasma channel. Chapter 2 gives an overview of the theoretical background necessary for the understanding of this thesis. The generation of a hollow laser pulse and a simulation of the electron density evolution is described in chapter 3. The experimental setup and the used methods for the measurements are detailed in chapter 4. Results of these experiments to the creation of hollow plasma channels are presented in chapter 5. Finally, chapter 6 summarizes the results and gives an outlook to future experiments and applications.

Chapter 2

Theoretical Background

This chapter gives an overview of the theoretical background needed for the comprehension of the present thesis. The first section 2.1 deals with the description of laser pulses via Gaussian beam optics and gives a short introduction into the impact of beam phase onto the intensity distribution. Afterwards, a basic description of a plasma is given and important plasma parameters are introduced. Section 2.3 contains an explanation of ionization processes caused by a laser pulse. The last section describes the acceleration of electrons in a plasma wakefield and motivates the use and creation of hollow core plasma channels.

2.1 Gaussian Beam Optics

The electric field of an electromagnetic wave in the so-called paraxial approximation can be described by [10]

$$E(x,y,z,t) = u(x,y,z)\exp(-jkz)\exp(j\omega t) \tag{2.1}$$

with $k = \omega/c$ and c the speed of light. The paraxial approximation is made for light that propagates under a small angle with respect to the optical axis, such that $\tan(\theta) \approx \theta$, $\sin(\theta) \approx \theta$ and $\cos(\theta) \approx 1$. The amplitude u is a slowly varying function on the wavelength scale and has to satisfy the paraxial wave equation

$$\left(\frac{\partial^2}{\partial x^2} + \frac{\partial^2}{\partial y^2}\right) u - 2jk\frac{\partial u}{\partial z} = 0. \tag{2.2}$$

One class of electric field solutions to the paraxial wave equation are the Gaussian beams, which represent the ideal case for a real laser beam. The normalised field amplitude for a Gaussian beam during free space propagation with the beam waist ω_0 at $z = 0$ is given by [10]

$$u(x,y,z) = \frac{\omega_0}{\omega(z)} \exp\left(-\frac{x^2+y^2}{\omega(z)^2}\right) \exp\left(-jk\frac{x^2+y^2}{2R}\right) \exp j\Phi \tag{2.3}$$

with the phase

$$\Phi = \tan^{-1}\left(\frac{\lambda z}{\pi\omega_0^2}\right) \tag{2.4}$$

and the curvature of the phase front

$$R(z) = z\left[1 + \left(\frac{\pi\omega_0^2}{\lambda z}\right)^2\right]. \tag{2.5}$$

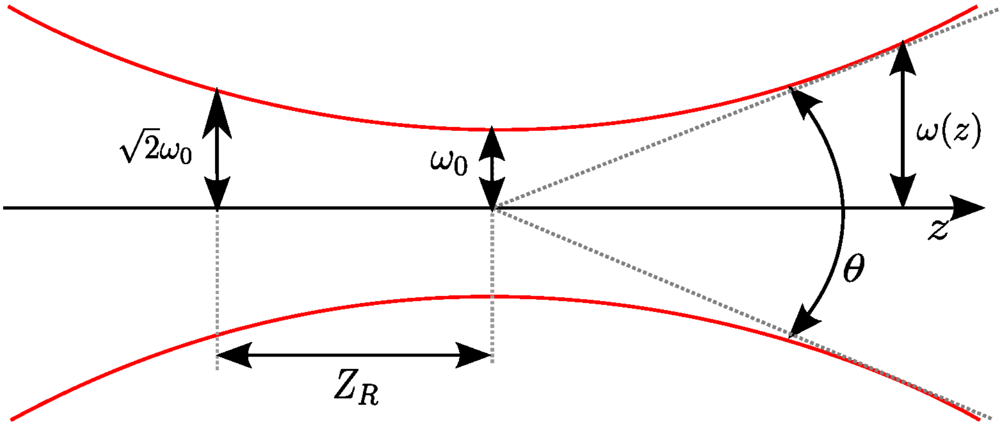

Figure 2.1: Sketch of the beam width $\omega(z)$ for a Gaussian beam. The beam waist ω_0, the Rayleigh length Z_R and the angle of divergence θ are indicated.

The transverse size of a laser pulse $\omega(z)$ during propagation in vacuum has a hyperbolic profile (compare figure 2.1). The radius of a Gauss beam gets larger with increasing distance from the focus:

$$w(z) = w_0\sqrt{1 + \left(\frac{z}{Z_R}\right)^2} \tag{2.6}$$

where $Z_R = \frac{\pi\omega_0^2}{\lambda}$ is the Rayleigh length and ω_0 is the radius at focus. Around its focal spot ($|z| > z_R$) the laser pulse diverges with the angle:

$$\theta_d = \frac{\omega_0}{Z_R}. \tag{2.7}$$

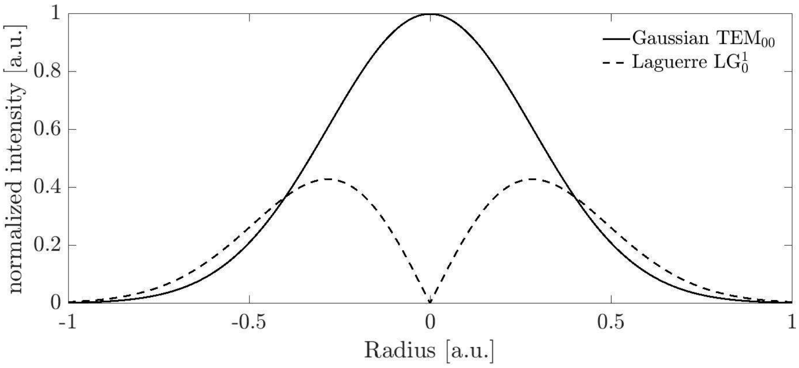

Figure 2.2: Transverse intensity profile of a Gaussian TEM$_{00}$ beam and a Laguerre LG$_0^1$ beam.

The Rayleigh length can be seen as a measure for the focusing strength of a laser. It indicates after which length the beam waist has increased by $\sqrt{2}$ to $\omega(z) = \sqrt{2}\omega_0$.

2.1.1 Laser Phase

The Gaussian beam is a solution to the paraxial wave equation. A superposition of a Gauss beam and an additional phase is still a solution to the wave equation and thus propagation invariant[11]. The Laguerre Gaussian (LG) beam is an example of such a superposition with a helical phase. The amplitude of the Laguerre Gaussian mode along its propagation is given by [12]

$$\begin{aligned} u_{p,l}^{LG}(r,\phi,z) = \frac{C^{LG}}{\sqrt{1+z^2/z_R^2}} \left(\frac{r\sqrt{2}}{\omega(z)}\right)^2 L_p^l \left(\frac{2r^2}{\omega^2(z)}\right) \exp\left(\frac{-r^2}{\omega^2(z)}\right) \\ \times \exp\left(\frac{-ikr^2 z}{2(z^2+z_R^2)}\right) \exp\left(i(2p+l+1)\frac{z}{z_R}\right) \exp\left(-il\phi\right) \end{aligned} \tag{2.8}$$

where C^{LG} is a constant and $L_p^l(x)$ are the associated Laguerre polynomials. For $l = p = 0$ the Laguerre polynomial is $L_0^0(x) = 1$ and equation 2.8 is equal to the Gauss mode. The intensity distribution of the LG$_0^1$-mode has a circular symmetry and is depicted in figure 2.2 in comparison to the Gaussian TEM$_{00}$ mode.

The transverse extent is dependent on l and is always larger than the Gaussian beam. Assuming the same energy in both beams, then the peak

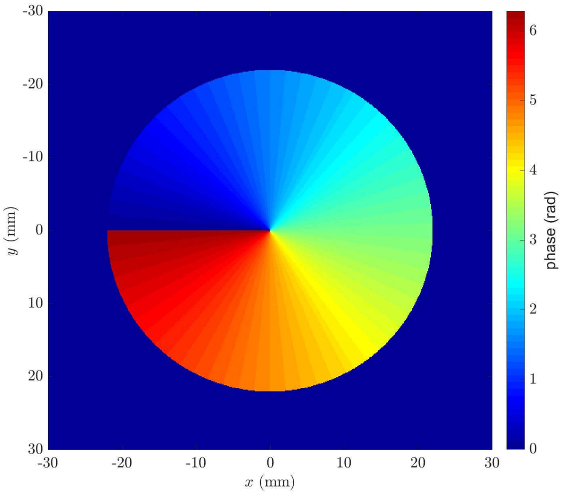

Figure 2.3: Phase map of a Laguerre Gaussian beam with $l = 1$.

intensity in the LG beam is lower.

In the center of an LG beam a phase singularity exists (compare fig. 2.3), which leads to the intensity minimum. This dark spot can be observed in the near and far-field as the beam is propagation invariant. The intensity maximum has the shape of a ring around the center but may be distorted due to phase modulations in the initial beam (see section 3.2.3).

2.2 Plasma Basics

2.2.1 Definition of plasma

The term plasma (Greek: moldable substance) is used to describe a state of a matter in which its charged constituents are separated from each other due to high energy influx. It consists of collectively behaving matter which has to have the following properties to be called a textbook plasma (for example in [13]):

1. *Spatial quasi-neutrality:* The volume of the plasma has to be large in comparison to the Debye shielding length λ_D.

2. *Temporal quasi-neutrality:* The time scale on which ordinary gas interaction happen is much larger than the electron plasma frequency

ω_p for charge shielding to occur.

3. *Ideal plasma conditions:* The number of charged particles inside the Debye sphere is greater than one ($\Lambda >> 1$) in order to provide collective behavior.

2.2.2 Debye Length

The Debye length is the characteristic length in a plasma on which the electrical potential of a local charge separation persists. In the proximity of a charge, there are statistically less charge carrier of the same polarity. This leads to a sheathing effect of the initial charge and to the plasma appearing electrically neutral on scales larger than the Debye length. The Debye length is defined by [13]

$$\lambda_D = \sqrt{\frac{\epsilon_0 k_B}{e^2}\left(\frac{n_e}{T_e} + \sum_{ionspecies} \frac{Z_i n_i}{T_i}\right)^{-1}} \tag{2.9}$$

where ϵ_0 is the electric permittivity in vacuum, k_B is Boltzmann's constant, n_e and T_e are the electron density and temperature, respectively. Correspondingly, n_i and T_i are parameters of the ion species with charge state Z_i. Due to their high mass the plasma ions can be considered immobile and thus the Debye length can be written as:

$$\lambda_D = \sqrt{\frac{\epsilon_0 k_B T_e}{n_e e^2}} \tag{2.10}$$

Assuming a plasma density of $n_e = 10^{18}\,\mathrm{cm}^{-3}$ at an electron temperature of $T_e = 5 \cdot 10^4\,\mathrm{K}$ one calculates a Debye length of $\lambda_D = 15.4\,\mu\mathrm{m}$.

2.2.3 Plasma Frequency

When one assumes a small, one dimensional displacement of an electron inside the background plasma of infinitesimal distance δx the resulting electric field has a strength of $E_\mathrm{x} = -\frac{en\delta x}{\epsilon_0}$. This gives

$$m\frac{d^2\delta x}{dt^2} = eE_\mathrm{x} = -m\frac{ne^2}{\epsilon_0 m}\delta_\mathrm{x} \tag{2.11}$$

with the plasma frequency

$$\omega_\mathrm{p}^2 = \frac{n_e e^2}{\epsilon_0 m} \tag{2.12}$$

where m is the electron mass. Assuming a plasma density of $n_e = 10^{18}\,\mathrm{cm}^{-3}$ the plasma frequency is $\omega_\mathrm{p} = 1.773 \cdot 10^{-17} 1/\mathrm{s}$. This parameter describes the basic oscillation frequency of the so called plasma or Langmuir waves. It also defines the time scale of which collective electron effects happen. Again the ion motion is neglected due to their high mass compared to electrons.

2.2.4 Ionization Defocusing

The refractive index of plasma is given by

$$\eta_p = \sqrt{1 - \frac{\omega_p^2}{\omega_L^2}} \tag{2.13}$$

and thus is dependent on the electron density, where ω_L is the laser frequency. When a laser pulse travels through undisturbed gas it will ionize it depending on its local intensity. A focused Gaussian laser beam has an intensity distribution, where the intensity maximum is on axis and it falls off radially. The electron density behaves accordingly as it is dependant on the laser intensity and an electron density gradient is formed. Light rays traveling through the plasma will now be bent due to refraction. One can calculate the path a light ray takes by looking at the bending angle due to the refractive index [14]

$$d\theta = \frac{\partial \Delta\eta}{\partial r} ds \tag{2.14}$$

When substituting equation 2.13 the bending angle after traveling a distance L is given by

$$\theta = \frac{1}{2} \int \frac{\partial (n_e/n_c)}{\partial r} ds \tag{2.15}$$

Due to this effect, the laser is defocused depending on the plasma electron density. This prevents the laser pulse from reaching its maximum intensity and minimum beam waist.

2.3 Laser Based Ionization Processes

At laser intensities on the order of $10^{14}\,\frac{\mathrm{W}}{\mathrm{cm}^2}$ the field gets large enough to influence the Coulomb potential in atoms. Different mechanisms can be observed and will be discussed for increasing intensities in the following section.
A bound electron inside an atom will be exposed to a combination of Coulomb and laser field. The corresponding potentials are the ionization potential I_p and the ponderomotive potential U_p. To decide which process is dominant

just from these two parameters, one can look at the comparing Keldysh parameter[15]

$$\gamma = \sqrt{\frac{I_{\mathrm{p}}}{2U_{\mathrm{p}}}} \tag{2.16}$$

which distinguishes between photo ionization and ionization by strong fields. For $\gamma >> 1$ photo ionization is dominant, while at strong intensities and of $\gamma << 1$ tunnel ionization or barrier suppression ionization are the leading effects.

2.3.1 Photoionization

Photoionization describes the process of energy absorption, where the total energy of photons $E = \frac{hc}{\lambda}$ is transferred to electrons in the atomic field. When enough energy is transferred to exceed the Coulomb potential the electron will become free with surplus energy being its kinetic energy (fig.2.4). For laser pulses with high fluence, more than one photon can be absorbed by a single electron. In that case, the electron can be separated from the atom by absorption of two or more photon energies simultaneously. The total energy of all absorbed photons is enough to ionize the atom even though the energy of a single photon would not have been sufficient. This process is called multi-photon ionization.

2.3.2 Tunnel Ionization

With increasing laser intensity the influence of the laser field on the ionization processes increases. The Coulomb field is deformed by the laser generating a barrier of finite thickness around the potential well. This allows the trapped electrons to tunnel through that barrier (see figure 2.4 (b)). The ionization rate for the tunnel ionization can be described by the Ammasov-Delone-Krainov (ADK) theory[16]. It is an analytic approach to describe the ionization rates of atoms in oscillating electromagnetic fields. The ionization rate for linearly polarized light is given by

$$\Gamma_{ADK}^{lin} = \sqrt{\frac{3(n^*\sqrt{I})}{\pi Z^3}} \frac{\sqrt{I} D^2}{8\pi Z} \exp\left(-\frac{2Z^3}{3(n^*\sqrt{I}}\right) \tag{2.17}$$

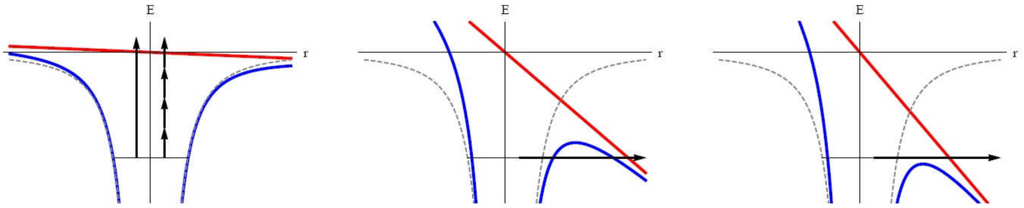

(a) Photoionisation (b) Tunnelionisation (c) BSI

Figure 2.4: Illustration of the different ionization processes.

where $n^* = \frac{Z}{\sqrt{2E_I}}$ is the effective principal quantum number and $D = \left(\frac{4eZ^3}{\sqrt{I}(n^{*4})}\right)^{n^*}$. For circular light the formula becomes

$$\Gamma^{circ}_{ADK} = \frac{\sqrt{I}D^2}{8\pi Z}\exp\left(-\frac{2Z^3}{3(n^*\sqrt{I}}\right) \tag{2.18}$$

These equations have a limited region of validity. For high laser intensities which are higher than the intensity needed for barrier-suppression ionization the ADK theory overestimates the ionization rate due to the Stark effect, where an electric field shifts atomic energy levels.

2.3.3 Barrier Suppression Ionization

For even higher laser intensities the Coulomb potential will be lowered under the ground-state energy level (see figure 2.4 (c)). The electron can escape the potential and leaves the atom ionized. This process is called barrier suppression ionization (BSI).
The required intensity is given by[17]

$$I_{BSI}\left[\mathrm{W/cm^2}\right] \geq 4.0\cdot 10^9 \frac{I_P\left[\mathrm{eV}\right]^4}{Z^2}. \tag{2.19}$$

For atomic hydrogen with an ionization potential of $I_\mathrm{p} = 13.6\,\mathrm{eV}$ and $Z = 1$ the BSI threshold intensity is $I_{BSI} = 1.4\cdot 10^{14}\,\mathrm{W/cm^2}$. Considering that the focused laser field is on the order of 10^{17} to $10^{18}\,\mathrm{W/cm^2}$ barrier suppression ionization is the dominant ionization process in most of the cases described in this work.

2.4 Plasma Based Acceleration

In this chapter, the concept of plasma-based wakefield acceleration is discussed (for a more thorough review see for example [2]).
When an electromagnetic driver, an intense laser pulse or a relativistic electron bunch, propagates through a plasma it excites plasma waves. The field expels electrons radially from the propagation axis. Due to their higher mass ions stay at their position and are considered to form a static background. This leads to the laser leaving behind a region of positive electric charge created by this background. The electrons are attracted by this electric field and oscillate around their starting position. An electron density modulation is formed on axis, with a peak behind the positively charged region. This plasma wave structure following the driver is called wakefield. The longitudinal electric field, that is formed by the density modulation - negative charge at the location of the electron density peak and positive charge at the ion background - can be used to accelerate particles. The electric field of the electron plasma wave is on the order of $E_0 = cm_e\omega_p/e$, or $E_0\,[\mathrm{V/m}] \simeq 96\sqrt{n_e\,[\mathrm{cm}^{-3}]}$ with the electron plasma frequency ω_p and the electron density n_e. Assuming a plasma density of $n_e = 10^{18}cm^{-3}$ the maximum field is $E_0 \approx 100\,\mathrm{GV/m}$. This field is approximately three orders of magnitude higher than that of a conventional radio frequency cavity, where the interaction of the field with the cavity walls limits the field strength.
The accelerating electric field has a sinusoidal structure in the linear regime. Figure 2.5 shows longitudinal electric field. Electrons can be inserted in front of the peak at the back of the wakefield and will be accelerated under the right conditions. The transverse electric fields are shown in figure 2.6. To accelerate an electron bunch in the wakefields, it needs to be placed in the accelerating phase of the longitudinal field as well as into the focusing phase of the transverse field.

2.4.1 Advantages of Hollow Plasma Channels

To prevent loss of beam quality when injecting an electron beam into a wakefield, the injected beam has to meet matching conditions. The transverse beam size has to be matched to the transverse focusing force in the wakefield and therefore to the plasma electron density. As the beam with constant size gains energy during acceleration the focusing forces have to be adjusted such that $k_\beta = \epsilon_n/(\gamma\sigma_x^2)$, where k_β is the betatron wavenumber of the focusing force, ϵ_n is the normalized transverse emittance, σ_x is the transverse beam size and γ is the beam particle energy[8].

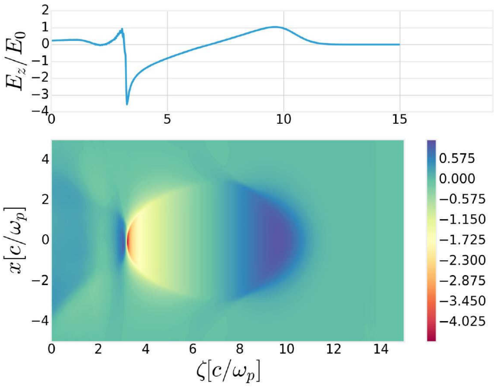

Figure 2.5: Schematic illustration of the longitudinal electric field from a HiPace simulation. From [18].

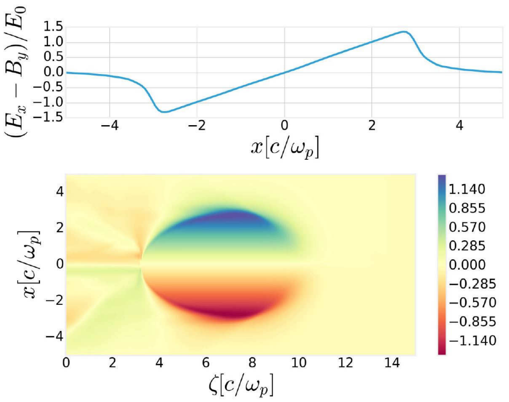

Figure 2.6: Illustration of the transverse electric field in a wakefield from a HiPace simulation.From [18].

This problem can be avoided with the use of hollow plasma channels, as they have beneficial properties. A hollow plasma channel has a limited or no electron density on the propagation axis and a peak electron density on a radius r around the axis. In this geometry, the transverse driver profile and the transverse profile of the accelerating wake are independent of each other. This consequently means that the accelerating gradient is transversely uniform and there are no transverse forces due to background ions or on-axis plasma electrons. A derivation of the transverse wakefields can be found in [20] and in [8].

In [19] the authors show that with a hollow plasma channel the focusing force can be controlled. They assume a non zero plasma density in the channel center and find that the accelerating force is controlled by the density in the channels wall n_w, while the focusing force is determined by the density in the channel n_c. Figure 2.7 illustrates this by comparing the longitudinal electric field (top) with the transverse focusing electric field (bottom) for different density ratios. The longitudinal field stays the same for different ratios while increasing the channel density increases the radial field gradient.

It is already experimentally shown, that such a hollow plasma channel can be used for the acceleration of a positron beam. Gessner et al. [21] created a hollow channel with 200 μm radius and accelerated a positron witness bunch with it. In a different work from Gessner [8], an in-depth theoretical analysis of the acceleration of electrons and positrons in a hollow plasma channel is given.

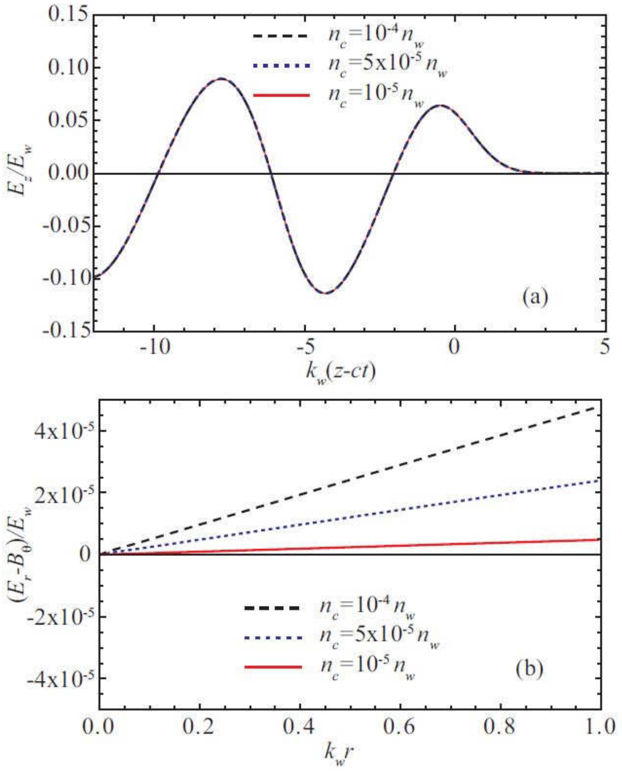

Figure 2.7: Longitudinal (top) and transverse (bottom) electric fields in a wakefield created in a near-hollow plasma channel. From [19].

Chapter 3

The Hollow Laser Beam

In this chapter, the generation of a ring-shaped laser beam is explained. Different methods are described to achieve such a laser shape in section 3.1. The chosen method, the spiral phase plate, is then simulated. The evolution of the laser pulse converted into the ring shape is calculated. With the obtained intensity profiles an electron density is calculated. Results from with simulations are shown in 3.2.4.

3.1 Generation of a Hollow Beam

There are several methods of creating a hollow laser beam experimentally. Some of which are introduced on the following pages.

3.1.1 Mode Conversion

Similar to the Gaussian (TEM) modes (compare chapter 2.1) there exist different sets of solutions to the paraxial wave equation (equation 2.2), for example Hermite-Gaussian (HG) and Laguerre-Gaussian (LG) modes. Any distribution can be described as a superposition of HG and LG modes with appropriate weighting.

The Laguerre-Gaussian (LG) solutions to the paraxial wave equation are given in equation 2.8 and are depicted in figure 3.1. The phase factor $\exp(-il\phi)$ is the source for the dark center of the LG modes.
These LG modes can be written as a superposition of another set of solutions to the wave equation, the Hermite Gaussian (HG) modes

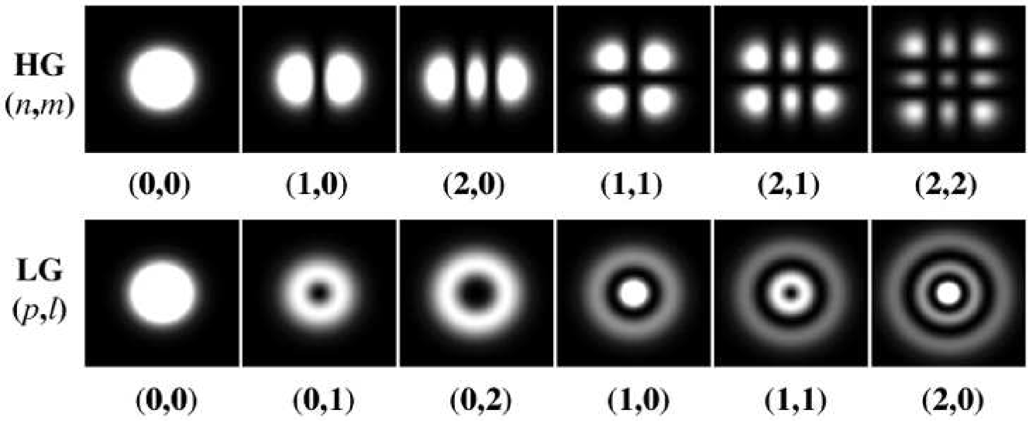

Figure 3.1: Transverse intensity distribution for the Laguerre-Gaussian and the Hermite-Gaussian solutions to the paraxial wave equation taken form [22].

$$\begin{aligned} u^{HG}_{n,m}(x,y,z) = \frac{C^{HG}}{\omega(z)} \exp\left(-ik\frac{(x^2+y^2)^2}{2(z^2+z_R^2)}\right) \exp\left(-\frac{x^2+y^2}{\omega^2(z)}\right) \\ \times \exp\left(-(n+m+1)\frac{y}{x})\right) H_n\left(\frac{\sqrt{2}x}{\omega(z)}\right) H_m\left(\frac{\sqrt{2}y}{\omega(z)}\right) \end{aligned} \tag{3.1}$$

where $H_n(x)$ and $H_m(y)$ are the Hermite polynomials of order n and m, respectively. LG modes can be transformed into HG modes via [23]

$$u^{LG}_{n,m}(x,y,z) = \sum_{k=0}^{N} i^k b(n,m,k) u^{HG}_{N=k,k}(x,y,z) \tag{3.2}$$

with the factor

$$b(n,m,k) = \sqrt{\frac{(N-k)!k!}{2^N n!m!}} \frac{1}{k!} \frac{d^k}{dt^k} \left[(1-t)^n(1+t)^m\right]_{t=0} \tag{3.3}$$

This transformation behavior can be used to create an LG beam experimentally [24]. The LG_{01} mode can be written as a superposition of the HG_{01} and the HG_{10} modes with a phase difference of $\pi/2$

$$u^{LG}_{0,1}(r,\phi,z) = \frac{1}{\sqrt{2}}\left(u^{HG}_{1,0}(x,y,z) + iu^{HG}_{0,1}(x,y,z)\right). \tag{3.4}$$

With the help of two cylindrical lenses, this mode conversion can be done when using a HG_{10} mode rotated by 45° with respect to the lens axis as

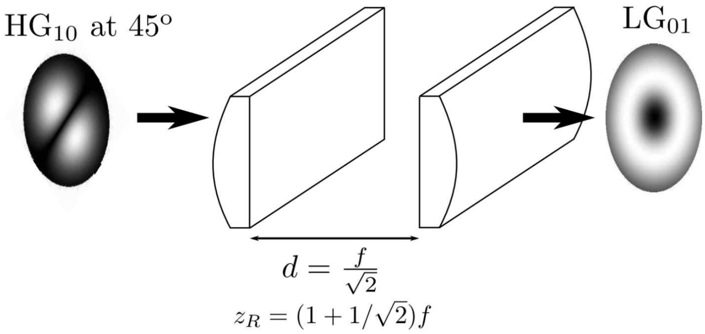

Figure 3.2: Setup of two cylindrical lenses to convert an HG input beam into an LG mode. From [25].

input. This rotated mode can be written as a superposition of HG_{01} and HG_{10} which are in phase. The phase can be shifted by $\pi/2$ exploiting the Gouy phase of the two modes [24]. For this, the following conditions have to be satisfied for the separation d and Rayleigh length z_R of the incoming beam.

$$d = \frac{f}{\sqrt{2}} \tag{3.5}$$

$$z_R = (1 + \frac{1}{\sqrt{2}})f \tag{3.6}$$

This technique for the creation of a hollow beam at FLASHForward is not desirable mainly due to the need for an HG input mode. The required HG mode could be created directly in the oscillator of the laser, but as this component is extremely sensitive to alignment changing it is not advisable. Furthermore, instead of creating HG modes in the oscillator one could directly create LG modes instead [26]. Since both methods require severe changes in the laser infrastructure they will not be discussed any further.

3.1.2 Axicon Generated Bessel Beam

Another family of beams - Bessel beams - was proposed and experimentally demonstrated by Durnin [27]. Bessel beams are suitable for the generation of a hollow plasma channel as shown by Fan et al. [28] for example.
Starting from the wave equations

$$\left(\nabla^2 - \frac{1}{c^2}\frac{\partial^2}{\partial t^2}\right) E(\vec{r},t) = 0 \tag{3.7}$$

and the specification for the intensity to obey

$$I(x, y, z \geq 0) = I(x, y) \tag{3.8}$$

the Bessel beam was derived with an electric field of

$$E(r, \phi, z) = A_0 \exp{(ik_z z)} J_n(k_r r) \exp{(\pm in\phi)} \tag{3.9}$$

where J_n is an nth-order Bessel function, k_z and k_r are the longitudinal and radial wave vectors, with $k = \sqrt{k_z^2 + k_r^2} = 2\pi/\lambda$. Figure 3.3 shows the intensity structure of a zeroth-order Bessel beam (left) with the intensity maximum on axis and a first-order Bessel beam (right). Higher order Bessel beams have a phase singularity on axis, resulting in an intensity minimum on axis. Bessel beams have the property of being diffraction-free, which means, that the intensity distribution does not diverge during propagation [29].

Such a Bessel beam can be created with an axicon, by giving the beam a conical wavefront. An axicon is a conical lens, which images a point onto a plane. Illuminating the axicon with a Gauss beam creates a zeroth-order Bessel beam. Higher order Bessel beams can be created by manipulating the phase of the incoming beam (for example see Andreev et al.[30]). One disadvantage of Bessel beams is that a lot of intensity will be transferred not only into the first maximum but also to the smaller maxima. This and the fact that axicons are generally very sensitive to alignment and need to be relatively close to the focus makes this method of creating a hollow laser beam uninteresting for FLASHForward. A variation of this method was used in recent experiments at the FACET beamline at SLAC National Accelerator Laboratory. Gessner et al. used a combination of a phase imprinting optic called kinoform and a modification of an axicon called axilens to create a high order Bessel beam ([21],[8]).

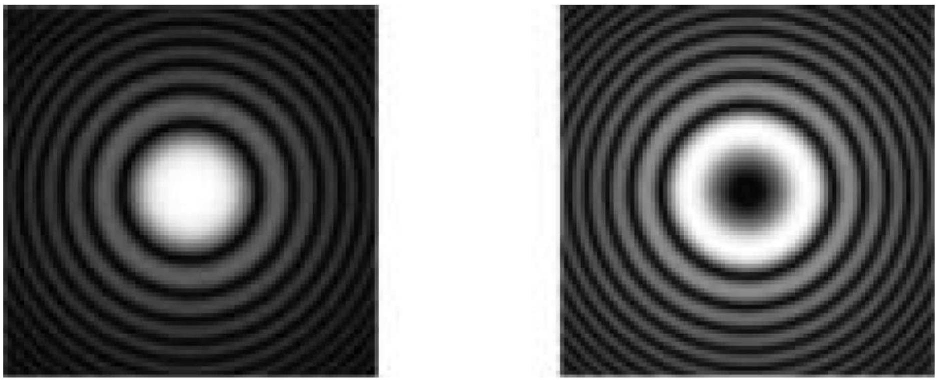

Figure 3.3: Intensity distribution of 0th (left) and 1st (right) order Bessel beams (from [29]).

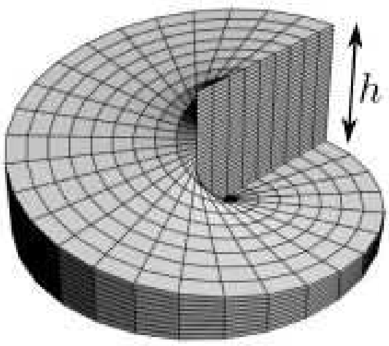

Figure 3.4: Illustration of a spiral phase plate from [25].

3.1.3 Spiral Phase Plate

A spiral phase plate (SPP) is a thin, transparent plate usually made from glass. This plate has an increasing thickness proportional to the azimuthal angle ϕ around the optical axis. Since the phase shift of light passing through material is directly proportional to the time it takes the light to pass through it, this spiral phase plate introduces a phase factor. The factor, which is a function of the azimuthal angle and reads $\exp{(il\phi)}$, is imprinted onto any beam incident on the phase plate. The topological charge l is determined by the following expression [31]

$$l = \frac{\Delta n \cdot h}{\lambda} \tag{3.10}$$

where Δn is the difference in refractive index between the SPP and its surrounding, h is the height of the step as depicted in the figure 3.4 and λ is the wavelength of the incident beam.

The phase changes continuously from 0 to $2l\pi$ with a round trip on any circle around the center of the (ρ, ϕ)-plane. For every point on this plane there has to be a point $(\rho, \phi + \pi/l)$. These two phases interfere destructively on the beam axis resulting in a dark spot in the center of the intensity distribution. A Laguerre-Gaussian beam (eqn. 2.8) is generated by this phase plate. Such a mode is propagation invariant, meaning that the intensity distribution does not change its general form during propagation except for divergence. Thus, the phase factor can be introduced to the laser pulse anywhere in the beam line, and it still exits after an arbitrary propagation distance. This makes this method very interesting for the FLASHForward project. The interaction point with hydrogen is more than 50 m away from the compressor output and the focusing optics produce a focal length of about 18 m. The phase plate can, therefore, be placed in front of the vacuum compressor which reduces the B-integral effect and the overall energy fluence in the SPP.

3.2 Simulating the Spiral Phase Plate

In this chapter, the effect of a spiral phase plate on the laser pulse is simulated. The intensity evolution in the focus is described and the electron density created by the laser is calculated. For the FLASHForward focus a setup with an effective focal length of $f = 17950\,\mathrm{mm}$ is planned. The following simulations will all be done using this setup.

3.2.1 Simulating the Phase Plate Effect on a Laser Beam

For the simulation of optical setups a widely used program is the ray tracing software ZEMAX. It takes the electrical field of light as input and calculates its propagation through a defined setup of optics. The input field can be chosen by the user to be a Gaussian laser beam for example. If the user knew the electric field of his desired input beam he could give any beam to this program.

The complex electric field of a laser beam can be calculated with a known amplitude u and a known phase distribution ϕ (compare eqn. 2.1). In order to simulate the effect of a spiral phase plate on the laser beam the phase factor $\exp(il\phi)$ can be added to the initial phase.

$$E_{spiral} = u_{initial} \cdot \exp\left(i\left(\phi_{initial} + \phi_{spiral}\right)\right) \tag{3.11}$$

The added spiral phase can be modified in order to see the effects of different topological charges l. The creation of a phase distribution is shown in figure 3.5, where the measured phase distribution from the laser acceptance test was used as a realistic initial phase. Due to computational limitations, the phase is approximated with 128 steps, instead of a continuous increase in phase.

After calculating the electric field with equation 3.11 the laser pulse intensity distribution is calculated by Zemax. At arbitrary propagation distances, the intensity distribution can be exported for further calculations.

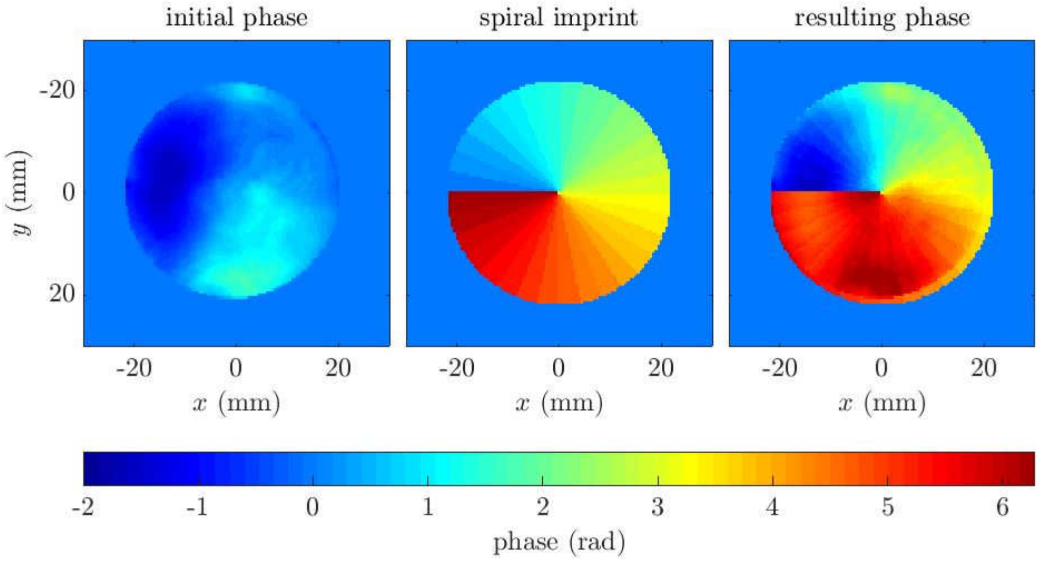

Figure 3.5: This figure shows how the input phase for the Zemax simulation were created. To the initial phase map (left) a spiral imprint (center) is added to create the final phase map (right).

3.2.2 Optimal Conditions

When using focusing elements the intensity distribution at focus depends on the input intensity and phase. To give a reference for simulations that converge from the optimal input parameters - a flat phase and a Gaussian intensity profile - the focus is calculated for these. Figure 3.6 shows the focus intensity of the beam after the phase was altered in the way explained in 3.2.1 to resemble the effect of the spiral phase plate. The intensity profile is shown 1 m around the focal plane. The Gaussian input beam has the form of a Laguerre-Gaussian in the focus. The ring shape is visible throughout the focus, while it is larger in front and after the focus. Therefore, the simulation is expected to work as intended.

3.2.3 Realistic Phase Distribution

As the phase of a laser beam seems to have an influence on the far-field distribution, it is interesting to see, what effect a realistic laser phase has on the focal spot. Therefore simulations were done with a realistic initial phase distribution (see left plot in figure 3.5). This phase distribution was obtained during the laser acceptance test of the 25 TW laser system from FLASHForward taken by the manufacturer Amplitude in France. Unfortunately, there

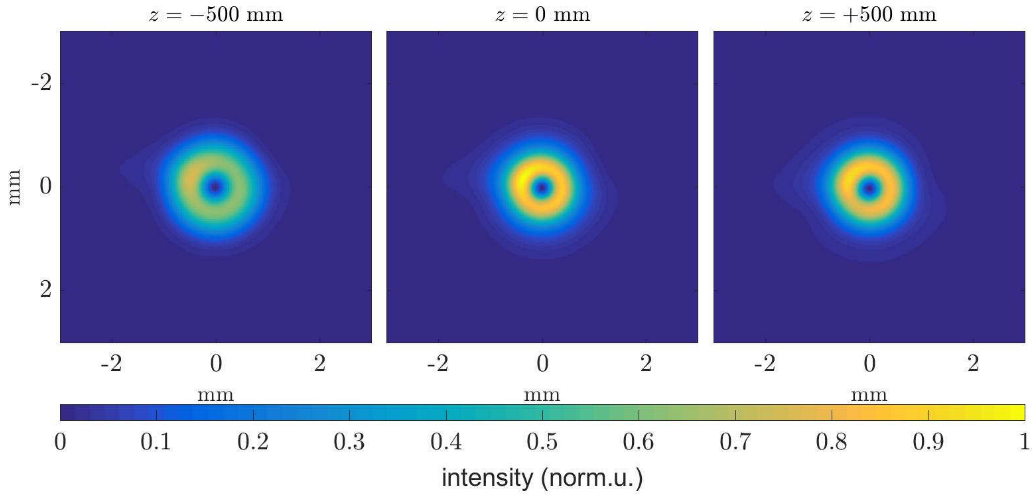

Figure 3.6: Intensity profile around the focus for near optimal input conditions of a Gaussian intensity and a flat phase.

is currently no way to measure the laser phase in the laboratory at DESY, so no recent phase distribution is available for this simulation.
Figure 3.7 shows the resulting focus before, at and after focus. The focus did not lose its hollow shape, but intensity shifted within the ring to create regions with high intensity and regions with low intensity. Furthermore, there is more energy in the diffraction rings especially in front of the focus.

Even though the central point is still without intensity and most likely will produce an electron density distribution with some sort of hollow shape, this pulse shape is only feasible for first testing experiments. The calculation of the electron density performed in this work relies on the Abel transformation (see 4.2.2 for a detailed explanation) which assumes rotational symmetry of the plasma column. Rotational symmetry around the central point is not given in this case. An alternative to the use of the Abel transformation is tomography. With this method, there would be no need to assume cylindrical symmetry, but one needs data from at least two angles. Afterwards, the electron density could be calculated by the use of the Radon transform. This method is in use in medicine as computer-tomography scans.
The initial phase of the laser has to be controlled and changed to a flat phase front. For this, a deformable mirror can be used and its implementation is already planned. Such a setup consists of a mirror with piezo movers on its back, which are able to deform the surface of the mirror slightly, thus changing the phase front. The phase front is recorded by a wavefront sensor

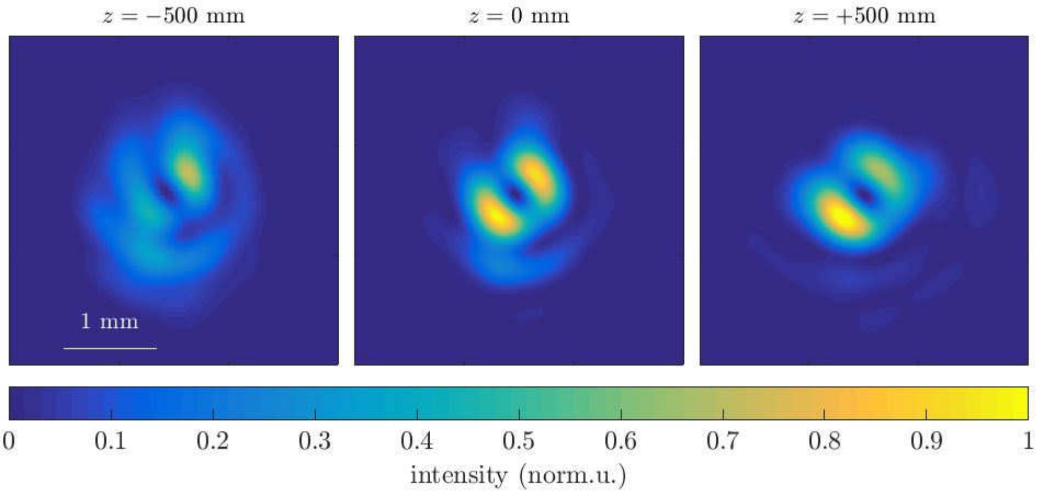

Figure 3.7: Simulation of the laser intensity distribution around the FLASHForward focus for a realistic initial phase distribution.

somewhere behind the mirror. In an iterative process a computer analyzes the measured wavefront and drives the piezo motors to compensate for errors. Depending on the speed of this process, it can compensate for static aberrations as well as dynamic aberrations.

3.2.4 Calculating the Electron Density

In this section, the laser intensity distribution is simulated for the FLASHForward experiment. The laser is focused by a combination of two lenses. This lens system has a effective focal length of 17950 mm. With the input beam thickness of 45 mm the focus parameters are calculated. The beam waist has a radius of 0.5 mm and the Rayleigh length is 660 mm long. The reason for this long and shallow focus is the structure of the desired plasma channel. The channel needs to be as uniform as possible, to have a constant plasma background for the electron driver. Another reason is the structure of the beamline. In order to couple the laser into the electron beamline one needs this distance to get the laser onto the same axis as the electron bunches. For a hollow channel this holds true as well.

Before showing the results from the simulation of the electron density, the method of calculation is introduced.
The laser intensity profile in the x, y-plane at a position z_i is given as $I(x, y, z_i)$. At each point, the electron density is calculated based on the

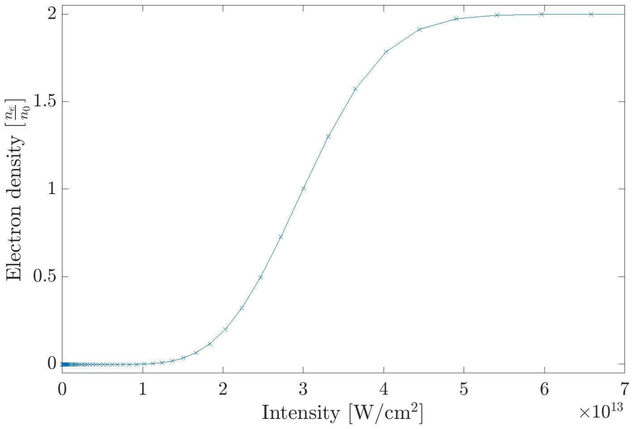

Figure 3.8: Relative electron density n_e/n_0 for a 25 fs laser pulse.

ADK ionization rate, which gives a probability for a hydrogen atom to be ionized by a certain intensity.

Figure 3.8 shows the relative electron density expected from a $\tau_L = 25\,\text{fs}$ laser pulse passing through atomic hydrogen[1]. The absolute intensity of the laser pulse is calculated from the counts F in the simulated intensity distribution with

$$I(x,y,z) = \frac{\mathrm{F}(x,y)}{\int \mathrm{F}(x,y)\mathrm{d}x\mathrm{d}y} \cdot \frac{E(z)}{\tau_L A} \tag{3.12}$$

with the total energy $E(z)$ at the propagation step z and the area of interest A. After each propagation step, the laser pulse will have less intensity for the next position z_{i+1}, due to the energy deposition into the gas. The simulation tries to account for energy loss but neglects the influence of other factors. One of the effects that could have an impact on the electron density distribution is plasma defocusing, which is explained in section 2.2.4.

Figure 3.9 shows a lineout of the electron density at every propagation step as an example of what an electron density looks like throughout the interaction. In this case an energy of 90 mJ with a gas pressure of 2 mbar was used.

As the radius of the hollow channel has an impact on the accelerating structure the radius at the focal point is calculated. The focal spot is marked as $z = 0$ in figure 3.9. To see if it is possible to manipulate the radius by varying parameters, simulations were performed for a range of parameters. The first thing that is interesting is the use of different topological charges for the phase plate. In the simulation the charges $l = 1 - 5$ were used. The

---

[1] The difference between atomic and molecular hydrogen ionization rates are discussed in the master thesis by Gabriele Tauscher[18].

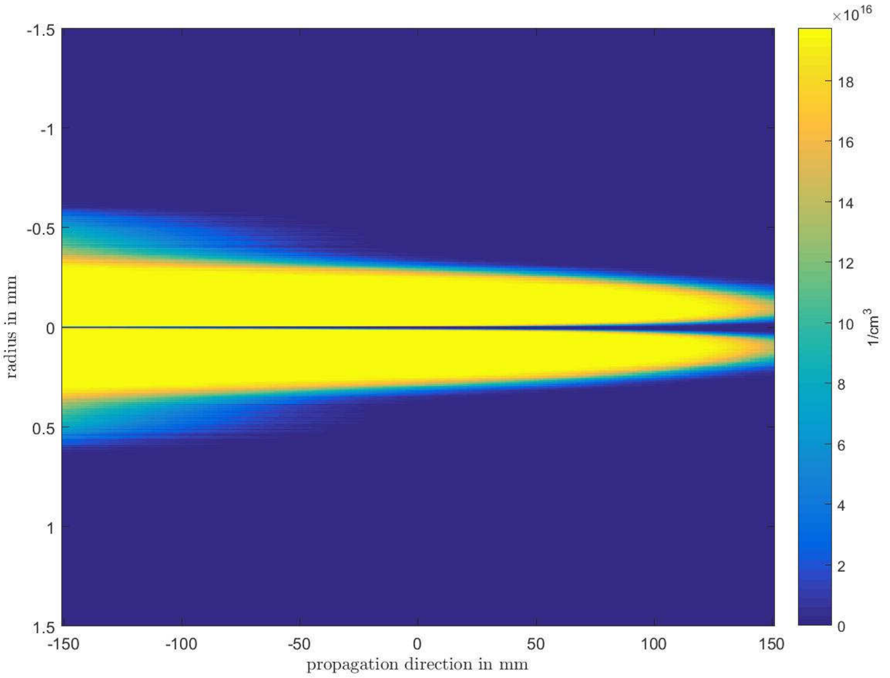

Figure 3.9: Longitudinal lineout of the electron density created by a laser pulse with $E = 90\,\mathrm{mJ}$, $l = 1$ at a gas pressure of $2\,\mathrm{mbar}$

second thing being investigated is how the change of laser energy changes the channels radius. Experimentally this is one parameter that is easily changed either by the insertion of neutral density filters or a rotatable polarizer, such as a $\lambda/2$-plate.

The last parameter to inspect is the pressure of the hydrogen the laser is interacting with. Depending on the setup of the gas target this is also easily changed by filling the gas reservoir with a higher pressure before releasing the gas into the vacuum chamber.

Behavior of the Channel Radius

As a first approximation, the loss of energy is neglected. The electron density is calculated solely based on the intensity distribution obtained from Zemax. Although this is not physically correct, it gives a rough estimate how the channel evolves for different laser pulse energies and different topological charges of the SPP.

The first parameter scan runs at a energy of $E = 120\,\mathrm{mJ}$ for topological charges $l = 1$ to 5. Figure 3.12 shows how the radius of the channel and the thickness of the channel wall at the focal point evolves for the different phase plates. In this plot, and in the following throughout this chapter, the inner radius is defined as the distance between the center and the point where density reaches $\exp(-2)$ of full ionization. Figure 3.10 shows a radial lineout of a sample electron density distribution. The red line indicates the threshold which defines the radius. The left crossing of the red line and the lineout defines the radius. The thickness is defined as the distance between the two crossings of red line and lineout. Lineouts are taken in x and y direction (compare figure 3.11) resulting in 4 radius values. From these, the average radius and a standard error are calculated.

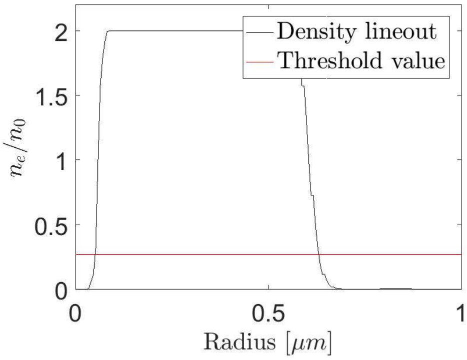

Figure 3.10: Sketch of the definition of the radius.

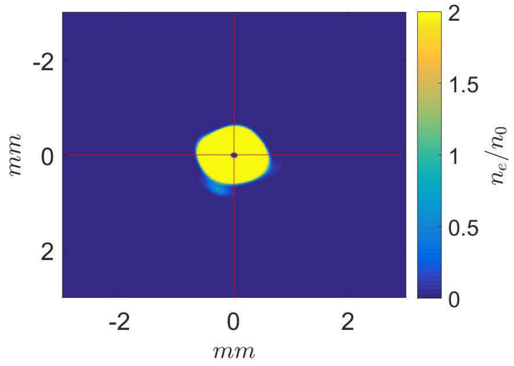

Figure 3.11: Illustration of how the radius is calculated in the simulations.

The topological charge of the phase plate has a strong impact on the radius. Increasing the topological charge by one increases the radius by 150μm on average. Higher order Laguerre-Gaussian beams indeed have a larger radius, so these results match the expectations. As the thickness of the wall stays constant, we can assume, that the intensity has to be distributed over a larger area. This leads to a lower peak intensity and may lead to energy depletion before ionizing the whole channel.

The second parameter scan for this first approximation is for the energy done for $l = 1$. Radius and thickness of the wall were calculated for energies from 30 mJ to 210 mJ. Figure 3.13 shows the results for the radius of the channel and the thickness of the channel wall. Increasing the energy decreases the channel radius, but not linearly like in the previous scan. The edges of the channel wall have a higher intensity, therefore areas which did not have enough intensity to ionize will now create a plasma and the radius decreases.

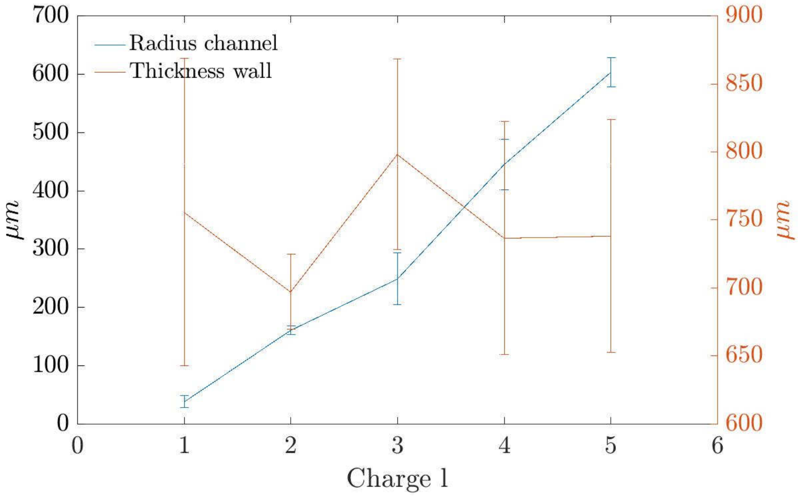

Figure 3.12: Radius and thickness of the hollow plasma channel for different spiral phase plate used. This figure shows a first approximation without considering energy loss.

The thickness on the other hand increases for the same reason.

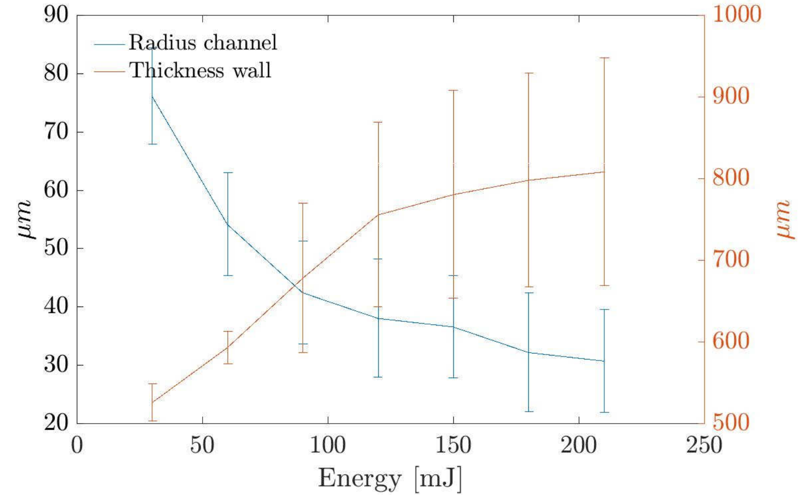

Figure 3.13: Energy scan in the plasma channel simulations. Radius and thickness of the channel are plotted against the tested energies without energy loss.

Energy Loss

The next step is to look at the evolution of the channel when one considers energy loss. After each plane (x, y, z_i), the energy for the next plane (x, y, z_{i+1}) is calculated, based on the loss due to ionization:

$$E(x, y, z_{i+1}) = E(x, y, z_i) - n_e V(x, y, z_i) E_{ion,pp}(x, y) \tag{3.13}$$

with the ionization energy loss per particle $E_{ion,pp}(x, y)$, the considered interaction volume $V(x, y, z_i)$ and number of particles n_e per cm^{-3}. The ionization energy per particle for hydrogen atoms is given by:

$$E_{ion,pp}(x, y) = 13.6\,\text{eV}. \tag{3.14}$$

Other effects, for example ionization defocusing (see section 2.2.4), are not accounted for, which may lead to an underestimation of the energy loss.
The topological charge scan including the energy loss introduced above is depicted in figure 3.14. The linear shape of the radius curve stays the same but increases its slope. Increasing the topological charge by one increases the channel radius by $\sim 200\,\mu$m. Due to the loss of energy during propagation, the plasma channel wall thickness decreases with increasing charge. Since the same start energy occupies a larger area the peak intensity in the wall is lower. This leads to a lower thickness for higher charges l.

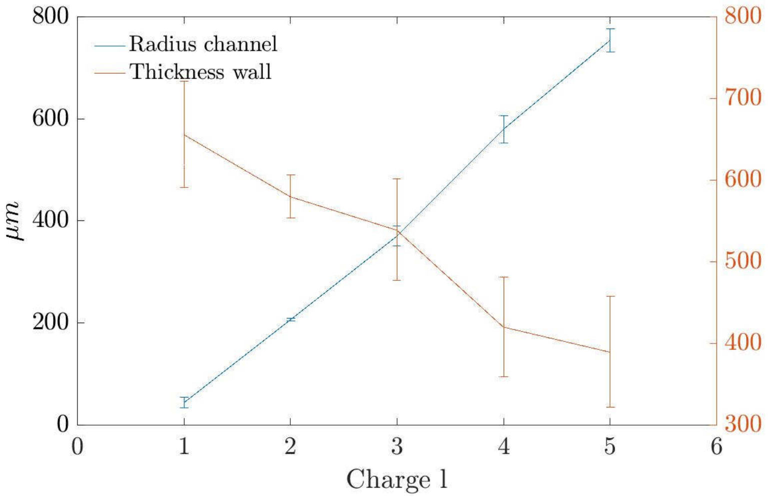

Figure 3.14: Radius and thickness of the plasma channel with an estimated energy loss during propagation.

The energy scan with accounted energy loss also has the same general relation between radius and energy (figure 3.13). Higher energies mean lower radii and larger wall thickness.

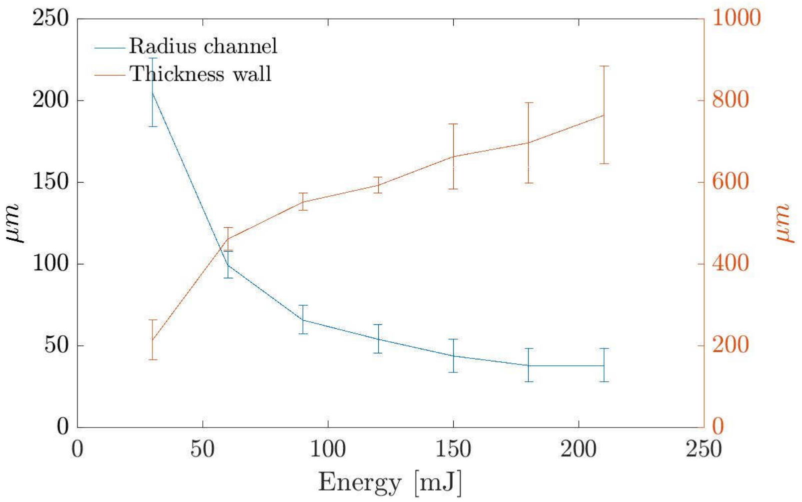

Figure 3.15: Energy scan with considered energy loss.

With the implemented feature of energy loss, the simulation can now also be performed for different pressures. At FLASHForward the pressures in the gas cell will be in the range $0.1 - 2\,\text{mbar}$. Therefore the simulations are performed in this range with an energy of 120 mJ and charge $l = 1$. Figure 3.16 shows the result for the radius at the focal spot. A linear dependency between radius and pressure is visible, but a much smaller one, than the charge scan showed. Increasing the pressure by 2 mbar increases the radius by around 20 μm. A higher pressure means, that there are more particles per volume the laser can interact with. Therefore the laser loses more energy, thus increasing the radius and decreasing the wall thickness.

Channel Evolution in Gas Cell

For the acceleration of electrons the hollow channel has to stay as constant in radius as possible. This will be investigated in this section. Therefore, the radius at the start of the 30 cm long gas cell ($z = -150$ in fig. 3.9) is compared to the radius at the end ($z = +150$ in fig. 3.9).
The change in radius for the energy scan is plotted in figure 3.17.

For low energies the laser loses a lot of ionization strength while propagating through of the gas cell. This manifests in the tripling of the radius at 90 mJ. Furthermore, for the simulation with 30 mJ and 60 mJ the radius at the end of the gas cell could not be calculated anymore, because the initially defined threshold for the radius was not reached. When creating a channel with a constant radius one needs to increase the laser energy so that the

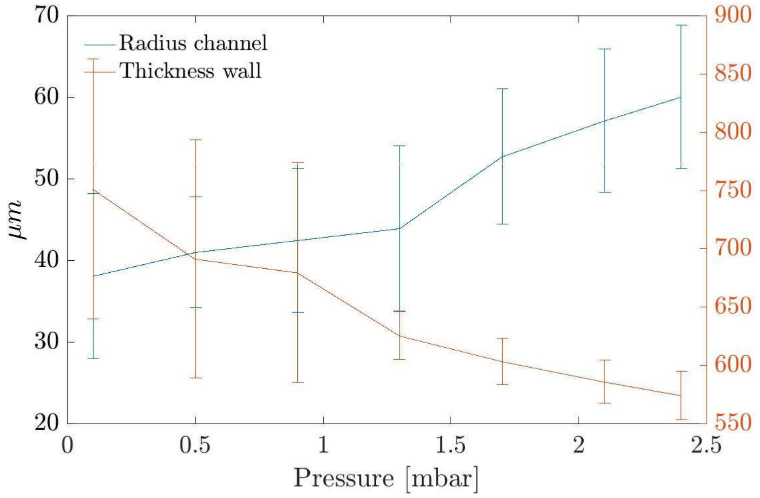

Figure 3.16: Radius and thickness of the plasma channel for different gas pressures. The energy loss approximation was applied.

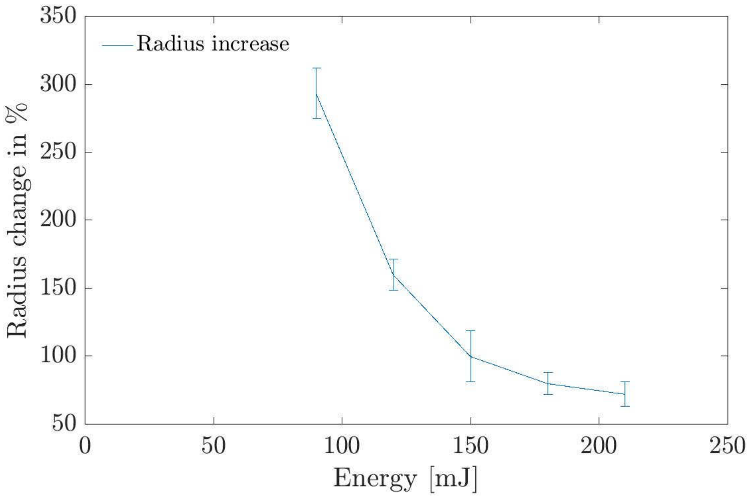

Figure 3.17: This figure shows the increase of the channel radius in % of the starting radius over a propagation distance of 30 cm for different starting laser energies.

energy loss during propagation is negligible.
A similar nearly exponential trend is visible in the change in radius for the pressure scan in figure 3.18. For low pressures the radius only changes on the order of 10 percent but for higher pressures the radius triples in size. This

is in line with our expectations. When more particles are available for the laser pulse to interact with, the more energy it will lose over a given distance. Thus increasing the radius more for higher pressures.

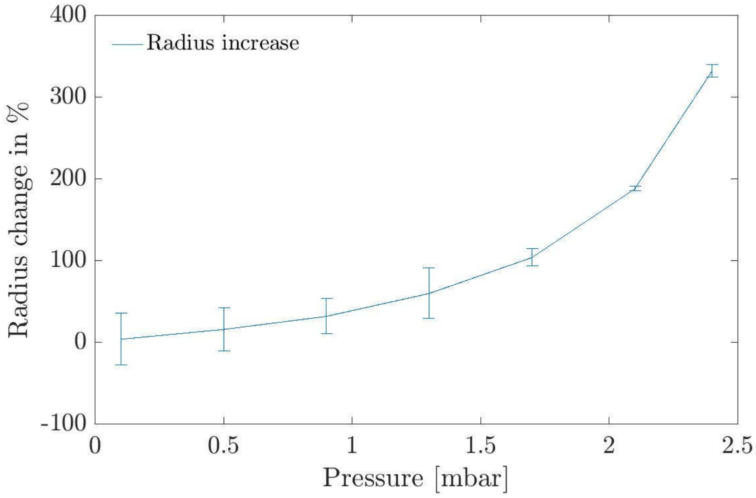

Figure 3.18: The increase of channel radius in % of the starting radius for different hydrogen pressures.

The calculation of the radius increase for the topological charge scan is a special case, as the energy of 120 mJ which was used, did not suffice to reach the threshold at the end of the gas cell. Therefore the threshold was reduced from the initial $\exp(-2)$ to 5% of full ionization for this calculation. The comparison with the other results is lost, but as the general evolution has a better visibility this step is justifiable.

With the reduced threshold for the charge scan, the radius increase is shown in figure 3.19. Higher topological charges have a lower radius increase than lower charges.

Conclusion from Simulations

The present simulations show the behavior of the electron density evolution of a plasma generated by a hollow core laser beam. Scans for the laser energy, the topological charge of the phase plate and the hydrogen pressure were performed.

The general range of the channel radius has to be defined by the charge of the phase plate, as this changes the radius the most. Minor changes to the radius can then be done with energy and pressure. Using a higher

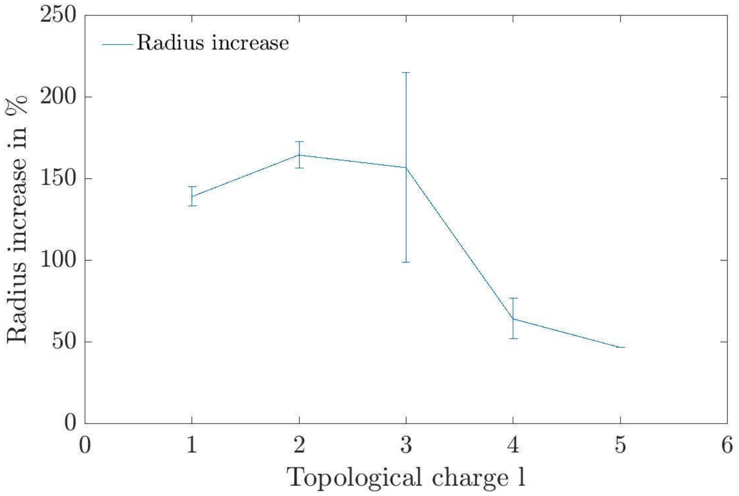

Figure 3.19: The increase of the channel radius is plotted for different topological charges of the spiral phase plate.

laser energy generally decreases the channel radius, while a higher hydrogen pressure increases the radius.
When looking for a plasma channel, which has a constant radius throughout the gas cell, the use of high laser energies seems plausible. Furthermore, the pressure should be decreased as far as possible. In real experiments the pressure gives little flexibility as it is chosen according to conditions for the plasma acceleration. One can instead use a higher charge of the used phase plate, which also minimizes the increase in radius.

For FLASHForward a good starting point for future experiments is the use of a phase plate with topological charge $l = 2$ at an energy around 200 mJ. The electron beam waist is on the order of $\sigma_x = 10\,\mu$m and has a position jitter of $10\,\mu$m [7]. Comparing this with the experiment done at FACET were the positron beam size is $\sigma_x = 50\,\mu$m[21] and the position jitter is $30\,\mu$m, where Gessner et al. used a plasma channel with a radius of $250\,\mu$m. Assuming the same dimension the channel radius at FLASHForward can be smaller, due to the smaller beam size. Assuming the smaller dimensions, a channel radius of around 190 mJ seems promising. Comparing 3.19, we see that for $l = 2$ the channel radius was around 210 mJ at 120 mJ. The radius can be lowered by using a higher energy (fig. 3.17), which also helps to keep the radius constant over the length of the gas cell. The overall extent of the plasma is then around 1.3 mm in diameter, which would be suitable for the current design of the gas cell with a diameter of 1.5 mm.

Chapter 4

Methods and Experimental Setup

This chapter gives an overview of the experimental setup and the different methods being used. The plasma electron density is measured with a probing interferometry setup. The first section 4.1 describes the laser system used at FLASHForward and its characteristics in the experiments. Afterwards, the plasma interferometry setup is explained and the data analysis process is described in section 4.2. In the last section, a computational method to estimate the electron density from a laser-intensity distribution along its propagation is explained. With a setup for a laser focus scan, the intensity evolution through the focus can be measured.

4.1 Laser Characteristics

4.1.1 FLASHForward Laser System

FLASHForward is a plasma-wakefield experiment located at DESY currently under construction. Its goal is to produce electron beams from plasma wakefield acceleration with energy at the GeV scale with sufficient quality for driving free-electron lasers. A 30 cm long hydrogen plasma will be created with a 25 TW laser, which is already installed and in use for LWFA experiments and ionization test experiments. This 10 Hz titanium-sapphire laser system utilizes the chirped pulse amplification (CPA) technique. CPA enables the generation of high-intensity laser pulses, as it avoids the destruction of laser beam quality, which may lead to damage of optics. Before passing the multi-pass amplifiers the pulse is temporally stretched, thus reducing the energy density. This technique uses light dispersion, the property of light having different phase velocities for different frequencies. After the amplification, the pulse can be recompressed again to then be of very high intensity and ultra-short duration. The FLASHForward laser consists of two amplifier stages and can produce pulses down to 25 fs short pulse duration at a central wavelength of $\lambda_L = 800\,\mathrm{nm}$ with a bandwidth around 80 nm. Additionally to the high power output with an energy of around 650 mJ the laser has a low energy output with 3.5 mJ which only passes the first amplifier. The experiments done for this thesis were performed with the aforementioned low energy output of the laser system.

4.1.2 Spiral Phase Plate for Hollow Beam Creation

For the creation of a hollow laser beam as a source for the hollow plasma channel a phase mask as described in section 3 is used.

The spiral phase plate (SPP) converts the Gaussian TEM_{00} mode of the FLASHForward laser system into a Laguerre-Gaussian LG_{0n} mode, where n denotes the topological charge of the optic. For this work, a SPP with a phase $\exp(in\phi)$ and $n = 1$ was used. It might be useful to perform similar experiments with higher topological charges, but for a first proof-of-principle experiment these SPPs are too expensive. The SPP was manufactured by the company SMOS[1]. The spiral structure is imprinted onto a quadratic glass substrate of 50 mm side length. The round spiral structure itself has a diameter of 45 mm and can therefore be used to transform both laser beams, either the low energy beam ($d \approx 14\,\mathrm{mm}$) or the high-energy beam ($d \approx 45\,\mathrm{mm}$).

In an ion exchange process silver atoms are inserted into the glass substrate. This is done while submerged in a silver nitrate bath with an applied electric potential at temperatures around 500°. The local silver ion concentration can be varied with a structured metal mask. With a higher silver concentration the refractive index is increased, thus being controllable by time and strength of applied potential. This process is not changing the surface structure of the glass and can be done with precision around $\frac{\lambda}{10}$.

The SPP was inserted into a Mach-Zehnder interferometer to verify it indeed changes the phase as expected from simulations (figure 4.1). The red circle in the center highlights the discontinuity, where a fringe splits up into two. This indicates a phase jump of 2π. Therefore, the SPP is expected to work as intended. This is also verified by figure 4.2 which shows the laser

---

[1] Smart Microoptical Solutions, http://www.smos-microoptics.de/

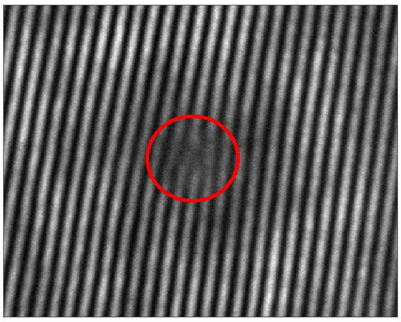

Figure 4.1: Interferogram of the spiral phase plate taken with a Mach-Zehnder interferometer.

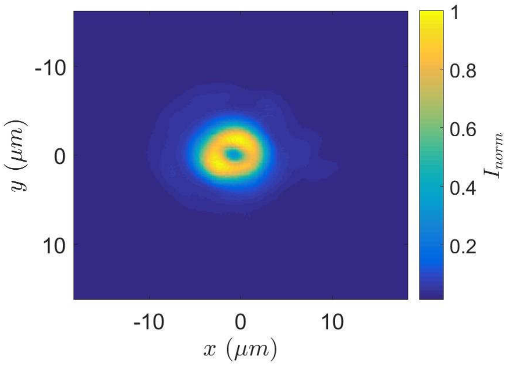

Figure 4.2: Camera image of the laser focal profile after passing the SPP.

far-field after transmission through the SPP. One clearly can identify the ring shape of the focus, which is also expected from simulations.

4.1.3 Laser Energy Measurement

The laser is subject to shot-to-shot fluctuations. These include fluctuations in energy, pointing, and pulse length. The laser energy determines the intensity distribution in the focal area where the plasma is created. The energy is the parameter most easily measured for each shot using a photodiode.
This diode[2] is placed behind the last mirror in front of the focusing lens. Light of every pulse is leaking through that mirror as the reflectivity is below 100 percent and will be observed with this diode. The created voltage of the detector is measured by an oscilloscope, which visualizes and saves the signal. A calibration measurement was performed in order to determine how a certain voltage signal transfers to the laser energy. As a calibrating tool an available energy meter[3] with a measuring head[4] was used.

Approximately 250 shots were taken for six energy settings on the diode while for the same time the energy meter collected shot energy data. To vary the intensity of the laser, neutral density filters were inserted in front of the low energy compressor. Filters with a neutral density of 0.1-ND, 0.2-ND, 0.4-ND, 0.5-ND and a combination of those leading to 0.8-ND were used.
After subtracting the background from the diode signal it was integrated

---

[2] Thorlabs DET36A - Si Detector

[3] gentec-eo Maestro

[4] gentec-eo QE50LP

Filter	E [mJ]	σ_E [mJ]	Diode signal [Vs]	Diode error[Vs]
0	2.9155	0.0899	1426.3	65.1
0.1	2.4905	0.0678	1236.9	57.4
0.2	2.0021	0.0638	1018.0	45.3
0.4	1.3803	0.0455	729.7	31.4
0.5	1.1865	0.0423	650.9	28.9
0.8	0.695	0.0230	460.2	23.1

Table 4.1: This table shows the results of the diode calibration measurement. For different filter settings data was taken with the energy meter and with the diode simultaneously. This data is shown with the corresponding standard deviations.

over the entire signal. Table 4.1 gives the results of the measurement.

From the data and graph 4.3 it is visible that there is a linear behavior between the integrated diode signal DS and the measured energy E. Therefore a linear regression was performed to get the conversion factor from diode data to laser shot energy. The linear regression yielded the following result for the energy and its standard error σ_E:

$$\begin{aligned} E &= 2.3262 \cdot 10^{-6} DS - 3.5415 \cdot 10^{-4} \\ \sigma_E &= 1.3494 \cdot 10^{-7} DS + 9.5658 \cdot 10^{-5} \end{aligned} \tag{4.1}$$

With these formulas it is now possible to calculate the energy for every recorded shot.

4.1.4 Measuring the Pulse Length

The pulse length is measured with a technique called "Grating-eliminated no-nonsense observation of ultrafast incident laser light electrical-fields" (Grenouille), which is used for ultrashort pulse length from about 20 fs to 180 fs.

The Grenouille generates and maps two information of the beam. A cylindrical lens focuses the incoming beam on the vertical axis onto a thick second harmonic generating (SHG) crystal. Because the crystal is hit under various incident angles it acts as a spectrometer and splits up the wavelength of the pulse in the y-direction. On the horizontal axis a fresnel biprism placed after the first lens splits the beam up in two beamlets. These overlap inside the SHG crystal such that the initial beam combines with itself again. Only where the two beams overlap a signal is generated, thus the beam delay is mapped horizontally, which is also known as self-gating. After passing through the

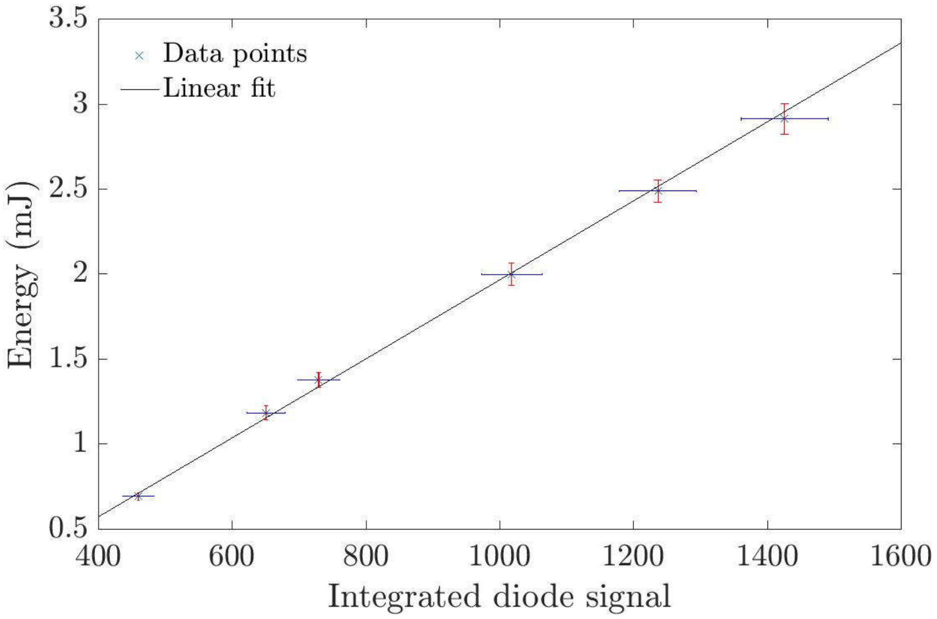

Figure 4.3: This graph shows the data for the diode calibration and a linear fit, obtained from a linear regression

crystal a second cylindrical lens images the signal onto a camera with the spectral information on the vertical axis and respective delay information on the horizontal axis. With this trace a phase-retrieval algorithm can match the complex electric field of the light pulse, from which the pulse length is deduced. Further information about the Grenouille can be found in [32] or [33].

The present measurements were done with a SwampOptics Grenouille 8-20-USB.

4.2 Plasma Interferometry

4.2.1 Experimental Setup

The experimental setup is shown in figure 4.4. The incoming laser beam is divided into two beams by a backside-polished mirror, which reflects over 99% into the plasma generating path (pump) and transmits less than 1% into the imaging path (probe). The pump beam propagates into the vacuum chamber after being focused by a $f = 150\,\mathrm{mm}$ focal length lens. The lens is mounted on a xyz-stage outside the chamber, so the focus can be moved

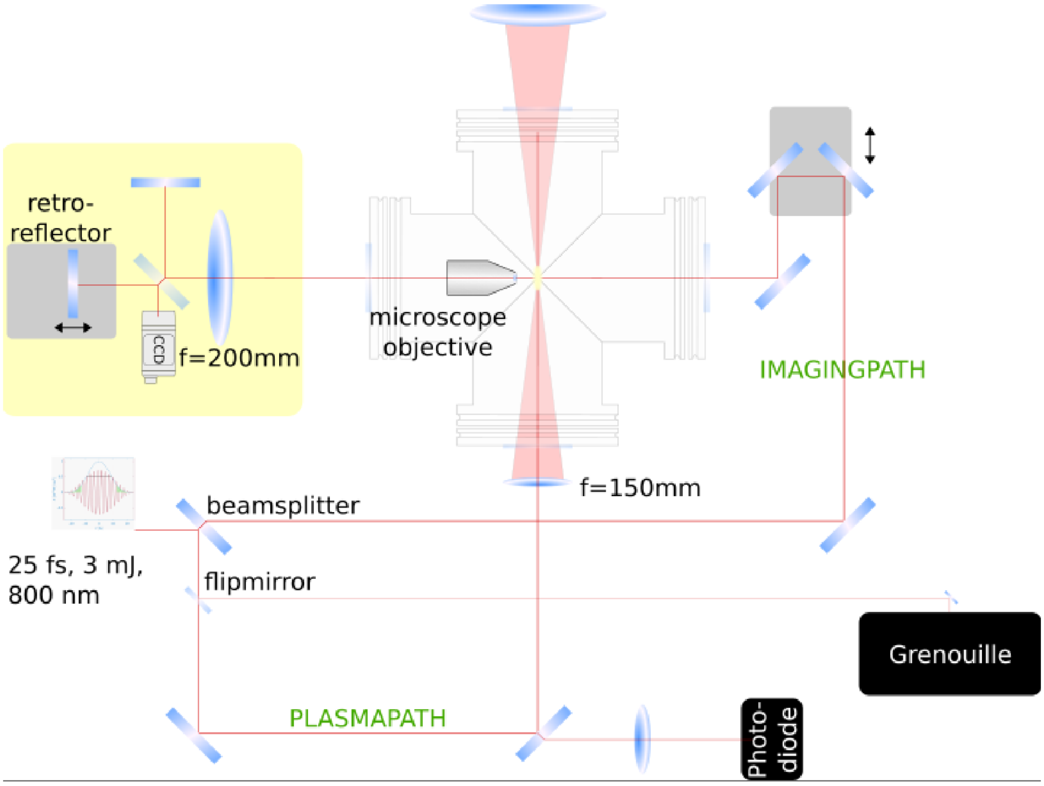

Figure 4.4: Overview of the experimental setup as described in the text (by courtesy of Gabriele Tauscher).

in z-direction. Behind the last mirror and before the plasma generating lens energy of each shot is measured by a photodiode (see 4.1.3). The spiral phase plate can be placed in front of the focusing lens. It can be translated transversely to the laser beam for alignment.

The probe beam is sent into the chamber under 90° to the pump and passes a delay stage in order to ensure the plasma is imaged around 3 ps after its creation. Also, the delay can be extended to observe the plasma expansion in time. After passing through the plasma the probe beam is imaged by an imaging system consisting of a 10x objective inside and a $f = 200\,\mathrm{mm}$ lens outside the chamber. The objective collects imaging photons diffracted by the plasma and the lens collimates the imaging beam. A Michelsen interferometer is the next component of the imaging path. It consists of a 50:50 beam splitting mirror, a plane mirror hit under 0° and a retro-reflecting mirror. The retroreflector inverts the beam at the horizontal plane. The two beams are recombined at the beamsplitter such that the top and bottom half each contain the plasma signal and reference light. This creates an interference pattern when the optical path length of both arms are equal. This interference pattern gives information about the phase difference created by the plasma and is imaged on a CCD camera. The size of the fringes depends on the angle between the two recombined beams.

In order to measure the resolution of the imaging system and the size one of the pixels of the interferometer camera is having on the imaging plane, a *1951 USAF resolution test target* from *Thorlabs* according to the *MIL-S 50A standard* is used. Imaging this target on the imaging plane, where the plasma will be observed, makes it possible to determine the pixel size and the resolution of the system. The target has lines printed onto it, with known size and distance to each other. Counting the pixels of a line on the image gives the pixel size on the detector. Doing so yields a pixel size of $0.510 \pm 0.039\,\frac{\mu\mathrm{m}}{\mathrm{px}}$. The resolution limit is determined by the contrast of the lines and the space between them. One possible criterion to determine the resolution limit is the Rayleigh criterion, which calls for a 26.3% [34] dip between two maxima in order to distinguish those two peaks. With this criterion, the resolution limit of the optical system is $4.9 \pm 0.4\,\mu$m.

Light propagating through a medium with higher refractive index than vacuum will have a longer optical path length $s = \eta c t$. This will result in a phase change of the light traveling through the plasma. From equation 2.13 follows, that the refractive index of plasma is lower than that of vacuum $\eta_{vac} > \eta_p$. Therefore, light passing through the plasma will have a lower phase shift. This phase shift can be written as $\Delta\phi = \frac{2\pi}{\lambda_L}(\Delta s_{vac} - \Delta s_p)$. The beam passing the medium will have its phase shifted with respect to the wavefronts passing the same optical path in vacuum. With the plasma refractive index (2.13) inserted the phase change can be approximated by

$$\Delta\phi \approx \frac{\pi}{\lambda_L}\int_L \frac{n_e(l)}{n_c} dl \tag{4.2}$$

This phase difference is called fringe shift and it is dependent on the plasma electron density n_e. From this measured fringe shift one can later calculate the electron density as is described in the next section.

4.2.2 Phase Retrieval and Abel Inversion

Extracting the phase information from the interferometry picture can be done following Takeda et al. [35].

The input fringe pattern is of the form

$$g(x,y) = a(x,y) + c(x,y)\exp(2\pi i f_0 x) + c^*(x,y)\exp(-2\pi i f_0 x), \tag{4.3}$$

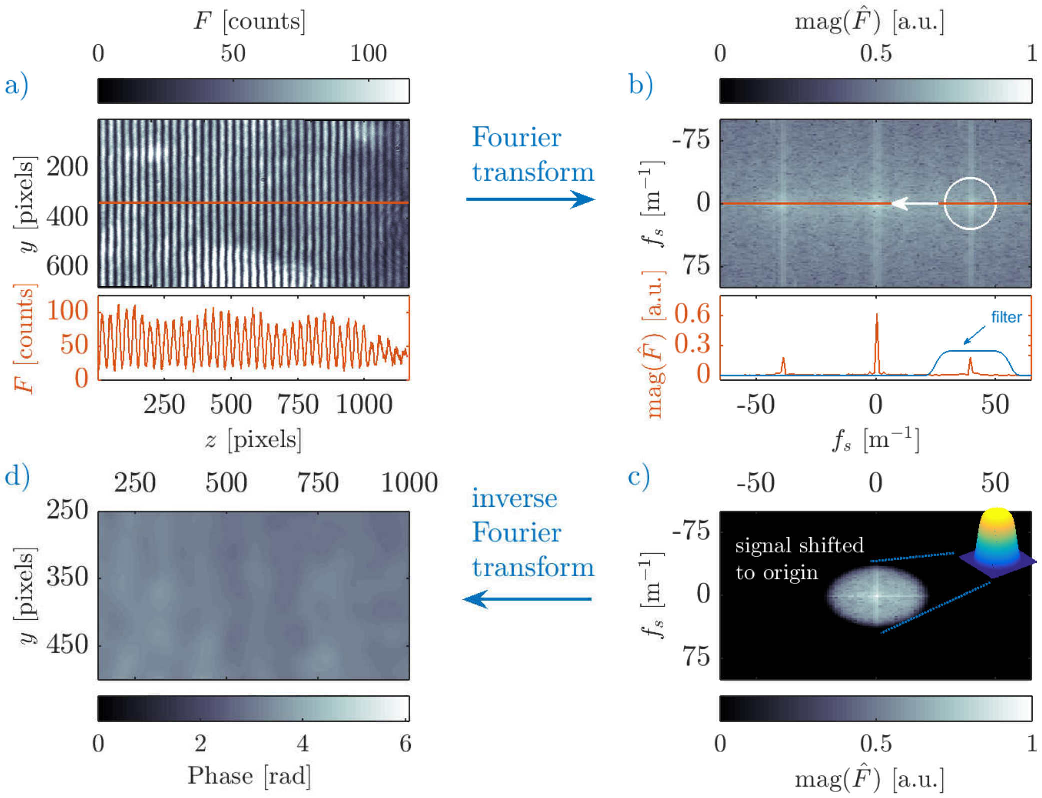

Figure 4.5: Overview of the phase retrieval process. The input fringe pattern a) is Fourier transformed into b). The spatial frequency is filtered out and moved to the center of the Fourier space c). The phase shift d) is obtained from the inverse Fourier transform. Illustration from [18].

where

$$c(x, y) = \frac{1}{2} b(x, y) \exp\left(i\phi(x, y)\right). \tag{4.4}$$

The desired phase information is in $\phi(x, y)$, while $a(x, y)$ and $b(x, y)$ are unwanted background variations and f_0 is the underlying spatial carrier frequency. To extract the phase information one starts by performing a fast-Fourier-transform (FFT) algorithm on the input data (fig. 4.5a)) and gets

$$G(f, y) = A(f, y) + C(f - f_0, y) + C^*(f + f_0, y), \tag{4.5}$$

with f as the spatial frequency in x direction, while A and C denote the Fourier spectra. In figure 4.5b) the Fourier transformed data is shown. The spatial frequency is visible in the center and the Fourier spectra are on the left and right side of it. The spatial frequency and the Fourier spectra can be separated. This can be done because the spatial variations $a(x,y)$, $b(x,y)$ and $\phi(x,y)$ are slow compared with f_0. After filtering out the background variation $a(x,y)$ one of the two signals on the carrier $(C(f \pm f_0, y))$ can now be separated and shifted to the origin (fig. 4.5c)) to obtain $C(f,y)$. Computing the inverse Fourier transform of $C(f,y)$ with the FFT algorithm one gets $c(x,y)$ from equation 4.4. Calculating the complex logarithm then gives the wanted phase in the imaginary part (figure. 4.5d)). This phase is indeterminate to a factor of 2π. The phase can be correctly calculated with the *unwrap* function in Matlab. This function looks for phase jumps greater than π and corrects the phase on these points by adding multiples of $\pm 2\pi$.

This phase retrieval fringe pattern analysis is done for the background pictures and the plasma pictures. Afterwards, the plasma phase shift is subtracted by the background phase. In the end the electron density can be calculated with the Abel transformation. The Abel transform calculates the shape of a 3D object with the measured line-of-sight integrated signal, or in other words the projection onto a plane. The only assumption made is that the object has a radial symmetry. As the phase shift $\phi(x)$ is a projection of a 3D plasma, which should be radially symmetric, the electron density distribution $n_e(r)$ is reconstructed numerically with the Abel transform [36]

$$\phi(r) = -\frac{1}{\pi} \int_r^R \frac{d\phi(x)}{dx} \frac{dx}{\sqrt{x^2 - r^2}}. \tag{4.6}$$

Bringing equation 4.2 to the form

$$\phi(x) = -\frac{2\pi}{\lambda n_c} \int_r^R n_e(r,x) \frac{r}{\sqrt{r^2 - x^2}} dr \tag{4.7}$$

makes it usable for the Abel transform which results in

$$n_e(r) = \frac{\lambda n_c}{\pi^2} \int_r^R \frac{d\phi}{dx} \frac{1}{\sqrt{x^2 - r^2}} dx. \tag{4.8}$$

Using equation 4.6 the electron density is finally given by:

$$n_e(r) = \frac{\lambda n_c}{\pi} \phi(r). \tag{4.9}$$

4.2.3 Laser Focus Scan

In order to compare the experimentally measured plasma shape with a theoretical prediction (compare chapter 3.2) the focus evolution is measured.

For a laser focus scan the plasma generating lens is moved upstream by approximately 10 cm. A CCD-camera on a motorized stage directly records the laser intensity profile along the propagation direction of the laser through the focal area. At the start of the plasma measurement a focus scan is performed for the laser beam with and without the SPP inserted. Over a distance of roughly 2 mm the motor moves in 100 steps. On every step the camera saves 20 images of the focus and 20 images of the camera background light.

Chapter 5

Results

In this chapter, the results from the performed experiments are shown. First, the laser focus scan is analyzed and a calculation of the expected electron density (sec. 5.1.2) from this scan is shown. The next section is explaining the experimental results from the plasma interferometry measurements. Section 5.3 describes the ionization text experiment for the plasma channel used in FLASHForward and explains why that experimental setup was not used in this work.

5.1 Laser Parameters

5.1.1 Pulse Length Measurement

For the calculation of the laser pulse length, traces for 100 shots were saved from the Grenouille measurement. The retrieval algorithm analyzed all of the stored traces. The used code works with an iterative process to minimize the retrieval error. Several different retrieval algorithms are included, switching to another one if the error is too large. As it is an iterative process, every time this code analyses a Grenouille trace it will calculate a different pulse length. Therefore, the code was run three times to have a larger sample size for a fit with a probability distribution.

The best fitting probability distribution is the generalized extreme value distribution[1]. The data points and the fit with the probability distribution are shown in figure 5.1. The mean value and the standard deviation obtained from that distribution are $\tau = (27.2 \pm 4.3)$ fs.

---

[1] This was found by using all pdfs included in Matlab. The interested reader will find information and references at https://en.wikipedia.org/wiki/Generalized_extreme_value_distribution.

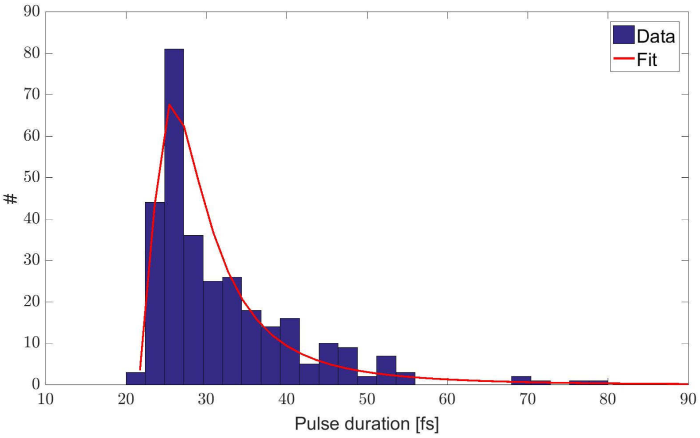

Figure 5.1: Pulse duration retrieved from the Grenouille traces plotted as a histogram. A probability distribution is fitted to the data points.

The Grenouille was set up about 2 m before the experimental chamber. Thus the pulse length is increased due to the further propagation in air as well as the plasma generating lens and the window before the vacuum in the chamber. The pulse broadening can be calculated from the group velocity dispersion (GVD) according to [37]. 2 m of air add approximately 0.14 ± 0.02 fs, the lens has a thickness of 5 mm and adds 5.5 ± 0.41 fs and the 3 mm thick window adds another 1.2 ± 0.1 fs. The pulse length at the interaction point with the hydrogen is approximately (34.04 ± 4.83) fs.

5.1.2 Laser Focus Parameters

A focus scan was performed as described in 4.2.3 for the two beam settings, one with and the other without the spiral phase plate. For every motor position the camera took twenty pictures throughout the laser focus. Background images were saved as well to correct the data for background light. Figure 5.2 shows the evolution of the unmodified beam in the focal region. The evolution of the hollow beam through its focal area is shown in figure 5.3. There is a distinct difference between the two beam modes. The beam without the SPP has a point-like focus. This behavior is expected from the Gaussian beam optics. The focus of the beam with the phase plate has a ring-shaped intensity distribution. The center of the focus has less intensity and around it there is an annular region of higher intensity. This intensity distribution is comparable to the Laguerre-Gaussian beam, with the difference, that this beam does not have zero intensity on axis.

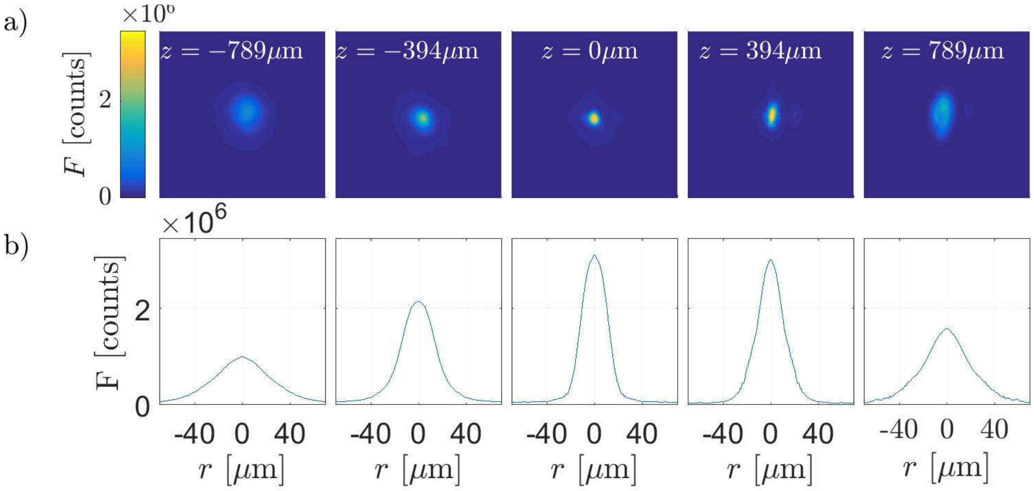

Figure 5.2: Intensity distribution throughout the focal region of the laser beam. The top row shows the beam intensity profile in counts. The bottom row shows the radially averaged lineout in counts.

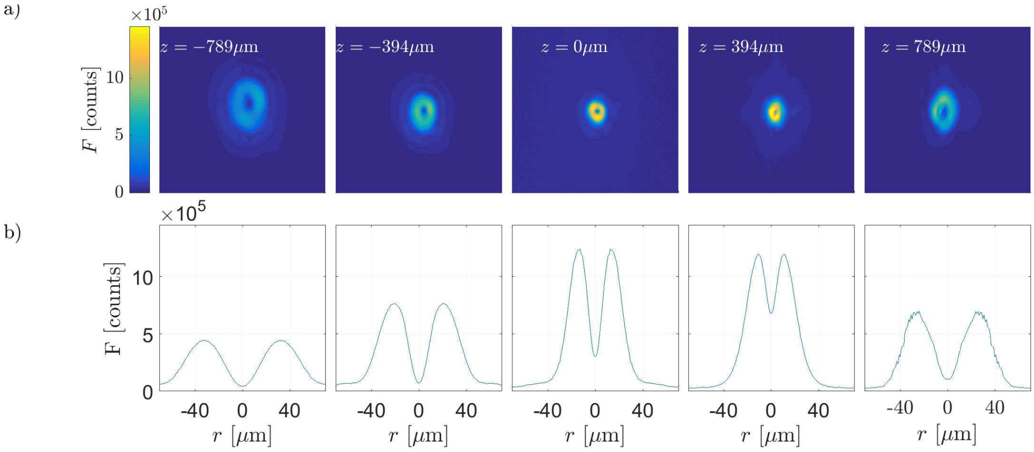

Figure 5.3: Evolution of the intensity distribution throughout the focal region of the hollow laser beam.

The radial evolution over the scanning distance is shown in figure 5.4

and in figure 5.5 for the unmodified and the hollow beam, respectively. For these plots, the images on every motor position were averaged and their background was subtracted. The center of mass was then calculated and the images were radially averaged. This procedure makes visualization easier but also averages out any asymmetries. The full-width half-maximum radius is plotted for every propagation step. For the hollow beam the inner radius is plotted in addition. Fitting a hyperbola on the data points allows us to calculate the focus parameters.

The beam waist for the unmodified beam is $\omega_0 = 8.11 \pm 0.94\,\mu$m and from the fit (see fig. 5.4)it follows that the Rayleigh length is $z_R = 131.74 \pm 1.96\,\mu$m. The outer beam waist of the hollow laser beam is $\omega_{0,outer} = 15.74 \pm 2.16\,\mu$m, while the radius of the inner region is $\omega_{0,inner} = 3.44 \pm 1.34\,\mu$m. The Rayleigh length of the hollow beam is $z_R = 159.49 \pm 1.99\,\mu$m, which is also obtained from the fit visible in figure 5.5. The focus of the hollow beam has a larger beam waist, which is expected from the theory when comparing a Gaussian beam and a Laguerre-Gaussian beam.

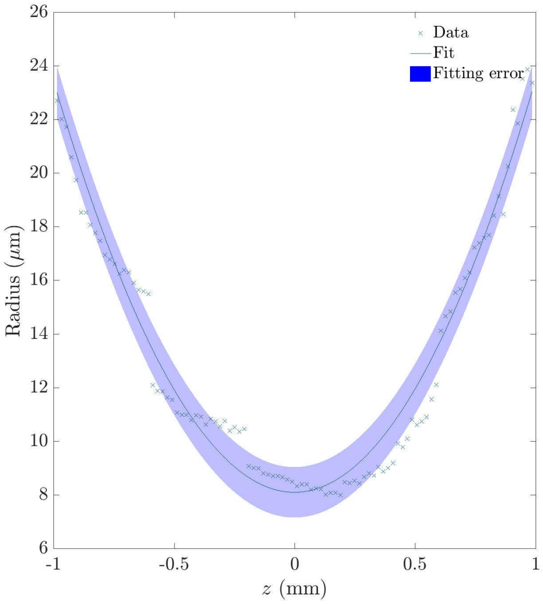

Figure 5.4: Half-width half-maximum radius on every propagation step for the normal beam with a hyperbola fit.

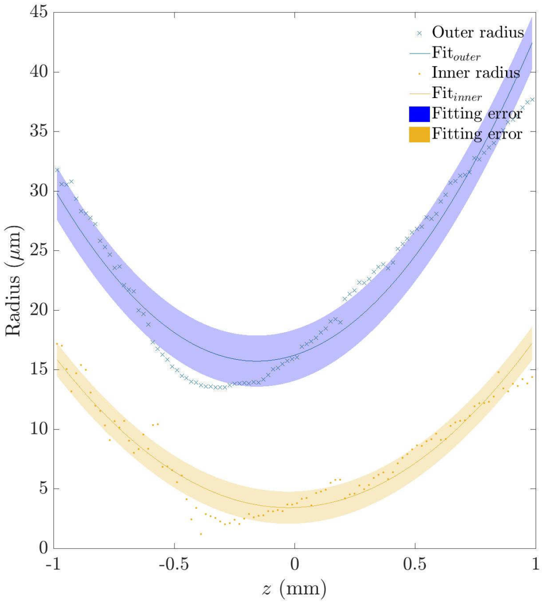

Figure 5.5: Half-width half-maximum radius on every propagation step for the hollow beam with a hyperbola fit. The outer radius is shown in blue and the inner radius of the hollow beam is shown in yellow.

Comparing of the Beam Modes

The hollow laser beam and the unmodified beam can be compared in terms of their shape. From the focus scan the intensity distributions from both beams (fig. 5.4 and 5.5) are compared at the same propagation step. For the following consideration, the intensities at z_0 of the unmodified beam were chosen. The beam without phase plate was filtered by additional 0.5ND, due to attenuation of the SPP. Furthermore, the spiral phase plate reflects a part of the laser beam. This loss due to reflection can be taken into account by correcting for the energy measured via the photo diode. The energies for the same filter settings with and without phase plate are compared. With the same filtering setting the phase plate energy was $E_{\text{SPP}} = E_0 \cdot (0.8833 \pm 0.0054)$. This was accounted for as well before continuing the consideration.
The center of mass was determined and the radial average around that point was calculated. Afterwards, the intensities were normalized to the maximum intensity of the unmodified beam.

Figure 5.6 shows the radial averaged and normalized distribution of intensity for the two beams. The maximum intensity of the hollow beam is

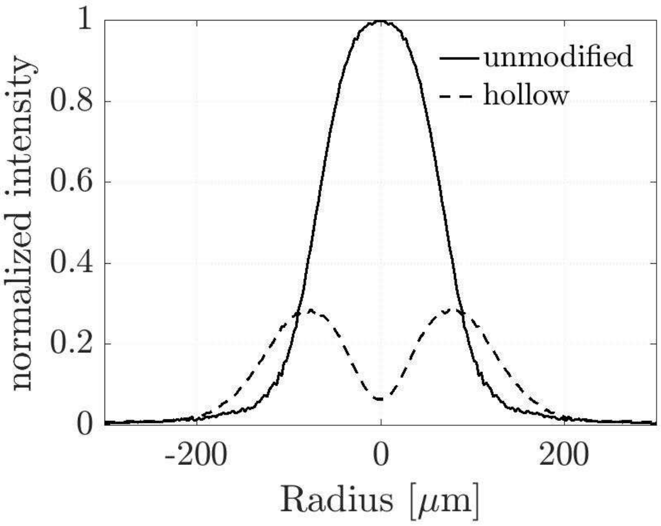

Figure 5.6: Comparison of measured beam intensity with and without spiral phase plate.

$I_{\mathrm{SPP}} = 0.2772 \cdot I_0$. With this information, the measured electron densities created by hollow beam and unmodified beam can be compared with each other. Comparing this result with the theoretically expected result, which is depicted in figure 2.2, shows, that the measured factor is lower than the expected of 0.4289. A few possible source for error come to mind. One factor could be the working principle of the phase plate. The phase increase by 2π around the axis is only viable for the design wavelength of 800 nm. As the laser has a spectral width of around 70 nm the efficiency is lowered. Another factor is the unmodified beam. As pointed out in 3.2.3 the laser phase has to be as flat as possible to create a uniform hollow beam, which might not be the case.

Strehl Ratio

The quality of an optical system is often times corrupted by aberrations[2], which are caused by optical misalignment or errors in optics. They prevent the laser to focus onto a point. A perfect optical system is only limited by diffraction over the aperture of the system. The intensity of the non-hollow beam in an optical system without aberrations and the measured intensity are compared in figure 5.7. A measure for the quality of the optical system is the Strehl ratio. It compares the intensity distribution of an unaberrated

---

[2] For further information about aberrations see for example [38]

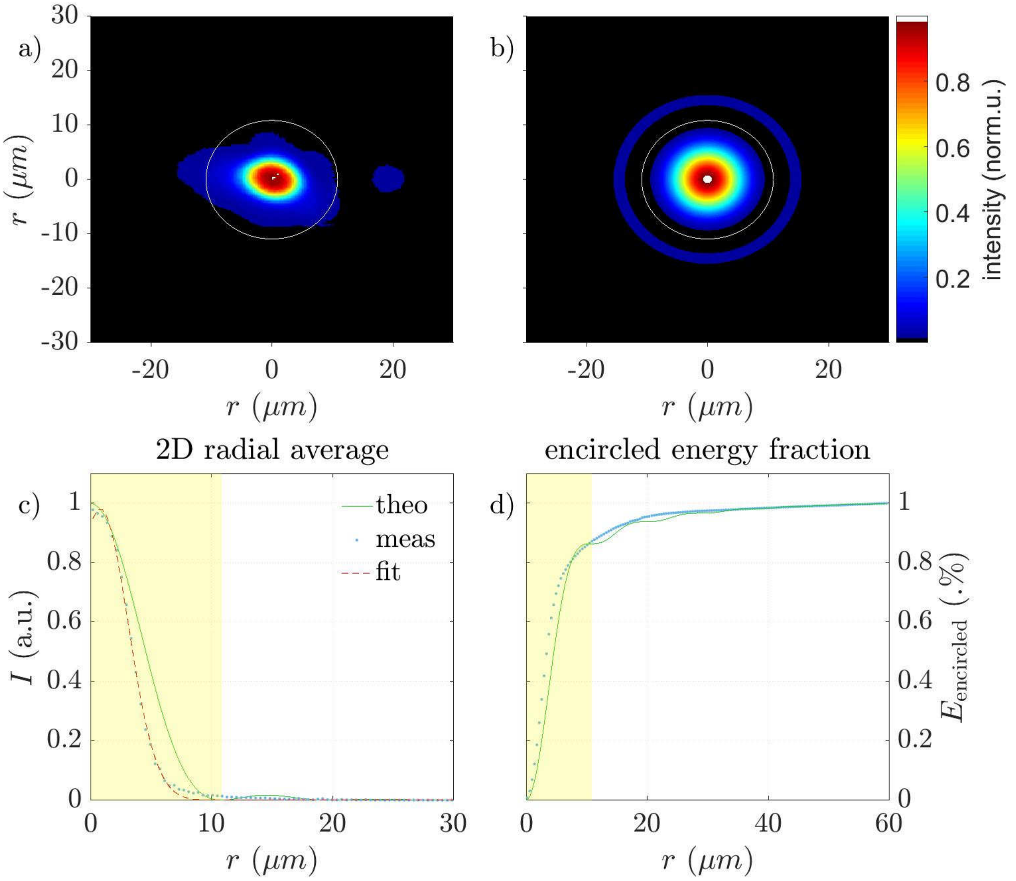

Figure 5.7: Illustration for the Strehl ratio. Image a) shows the focus spot of the laser beam. The Airy pattern expected from a perfect Gaussian beam is shown in b). Figure c) compares the radial average of the laser focus and the Airy disk, while the encircled energy is shown in figure d). The shaded area represents the radius at which the first theoretical minimum is reached.

beam, represented by the Airy disk (figure 5.7b)), with a measured intensity distribution (fig. 5.7a)). It takes values from 0 to 1, with 1 being a perfect optical system without aberrations.

In order to obtain the Strehl ratio of the optical system used in the experiments, either the maximum intensity of the focus or encircled energy within the first minimum of the theoretical profile can be compared. The theoretical radial average has a higher intensity between $r = 2\,\mu\text{m}$ and $r = 8\,\mu\text{m}$. Comparing the integrated area to the first minimum shown by the yellow area gives a Strehl ratio of 0.78 ± 0.047, where the error was estimated from the radial average. Figure 5.7d) shows the encircled energy fraction. The encircled energy fraction is higher for the measured intensity profile until a radius of $r = 9\,\mu$m.

Simulating Expected Electron Density from Focus Scan

The expected electron density can be simulated with the measured intensity data from the focus scans. Comparing the electron density obtained by this simulation with the measured electron density obtained from the Abel transformation of the interferometry data might show errors in either the simulation or in the data analysis. The electron density is simulated the same way as in section 3.2.4. The simulation was performed with an energy comparable with the energy used in the experiments shown later in this chapter. Figure 5.8 shows the electron density simulated from the laser focus scan of the unmodified beam with an energy of 0.9 mJ at a hydrogen pressure of 200 mbar. The electron density from the hollow laser beam is shown in figure 5.9 which was calculated with the same input energy and gas pressure. The radial average was calculated for better visualization. The expected radius at the beam waist of the channel of the hollow core plasma is calculated to $5.88 \pm 0.92\,\mu$m at the waist. The inner radius of the channel has a width of $1.12 \pm 0.22\,\mu$m, which increases to $4.76 \pm 0.71\,\mu$m over a propagation distance of 0.44 mm. The unmodified beam has a smaller expected radius (compare figure 2.2) for the same assumed peak intensity. In this simulation, the same initial energy was assumed. Therefore, the peak intensity of the hollow beam is lower than that of the unmodified beam. Nevertheless, the radius of the unmodified beam is $5.32 \pm 0.51\,\mu$m at the waist, which is smaller than the waist of the hollow beam. The higher intensity in the peak of the unmodified beam leads to a longer plasma channel, as the intensity falls below the ionisation limit later than in the hollow case.

The calculation of the electron density with the hollow laser beam shows, that the radius of the central region is very small. Detecting this small radius with the interferometry setup and being able to calculate it with the Abel transformation might turn out to be difficult. The interferometry setup, on one hand, is limited by the resolution of the optical system. The Abel transformation, on the other hand, relies on the rotational symmetry. The optical axis has to be set and deviations from it cause further errors in the calculations of the electron density. A plasma channel, which is not rotationally symmetric increases the error even further.

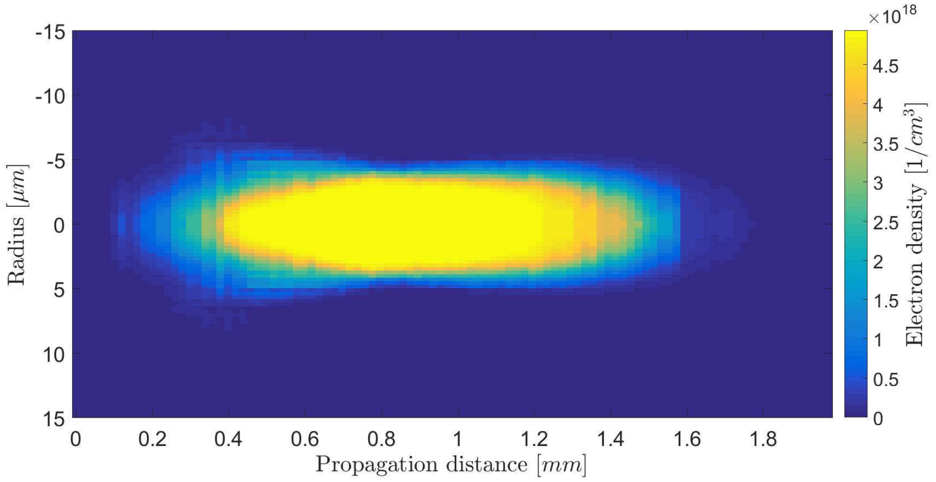

Figure 5.8: Electron density calculated from the measured laser intensity from the focus scan. The beam is not influenced by the spiral phase plate. The energy used in the calculation is 0.9 mJ. The laser is propagating from left to right in this figure.

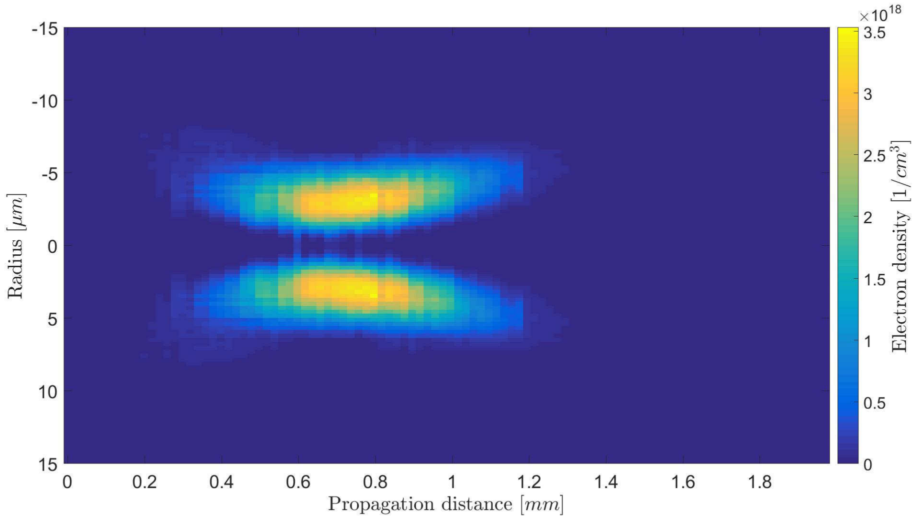

Figure 5.9: Electron density calculated from the hollow laser beam focus scan. The energy used in the calculation is 0.9 mJ. The laser is propagating from left to right in this figure.

5.1.3 Conclusion from Laser Focus Scan

The laser beam was successfully transformed into a hollow shape by the use of the spiral phase plate, which is visible throughout the focal region (figure 5.3). Nevertheless, the shape of the hollow laser beam could be improved. The initial phase distribution of the laser beam has to be flat and aberrations have to be avoided. This can be avoided by implementing an adaptive optic such as a deformable mirror. During alignment, it was also noticed that the focus could be significantly influenced by lens misalignment, up to a point where a ring-shape was no longer observable.

The simulation of the electron density shows that the hollow channel is very narrow. It might not be visible in the experimental measurement of the electron density. The inner channel diameter at waist is only around $3\,\mu$m, which is lower than the resolution of $4.9\,\mu$m in the employed optical setup (see section 4.2.1). At the start and the end of the plasma channel the inner diameter is around $10\,\mu$m and therefore might be visible in the measurements.

5.2 Electron Density Obtained from Plasma Interferometry

In this section, the results from the plasma interferometry are presented. From the simulation in chapter 3 we know that the radius of a plasma channel and its evolution is mostly influenced by the laser energy and the topological charge. Due to its cost, we only have a phase plate with $l = 1$ available. Therefore, the experiment is limited to a scan of the energy. The energy of the plasma generating beam was varied between approximately 0.3 mJ and 3.2 mJ, where the energy was measured as described in section 4.1.3. In order to know where the laser focus is located with respect to the field of view of the interferometer camera, shadowgraphy was used. When blocking one arm of the interferometer the plasma appears as a dark region on the camera. The vacuum focus of the laser is then expected to be at the location where only a point-like plasma is visible. The energy was reduced as much as possible while still being able to see the plasma on the camera. The center of the smallest visible plasma defines the vacuum focus point of the laser. The vacuum focus is marked as z_0 in the following images. It was found by fitting an ellipse onto the shadow of the plasma, where the centroid in z-direction is assumed to be the vacuum focus position. At the lowest energy setting the plasma still has an extend of over $400\,\mu$m, so accordingly, the error in the determination of the position of the vacuum focus is on the order of 100 μm.[3]

Afterwards, the setup was switched to the interferometry measurement and a set of data was taken at various energies for the two beam modes, unmodified and hollow. A second set of images was then taken after moving the plasma generating lens downstream, in order to image the beginning of the plasma. This was motivated by the fact, that the field-of-view of the camera turned out to be small compared to the plasma columns generated at higher energies.

5.2.1 Temporal Plasma Expansion

The experimental setup features the possibility to delay the imaging path with respect to the plasma generating path. This enables the observation of the plasma expansion.
The scan was performed with an average energy of $E = 2.8 \pm 0.27$ mJ with the spiral phase plate inserted into the beam path. The length of the imaging path was increased by 14.8 ± 0.3 ps between two measurements with the delay stage (see figure 4.4).
When looking at the radius of the plasma column one can estimate the thermal expansion. The maximal delay scanned with the increase of the imaging path length is 210 ps. The mean thermal velocity of hydrogen is calculated by $v_{th} = \sqrt{\frac{8k_BT}{\pi m_H}}$. Assuming hydrogen at room temperature it is

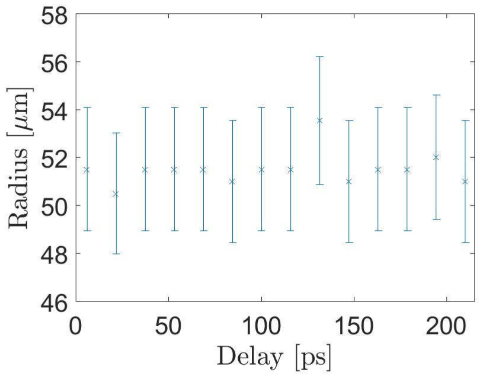

Figure 5.10: Radius at a propagation step in its temporal evolution.

---

[3] This method can be improved in future experiments by mounting the plasma generating lens onto a motorized stage. Performing a scan of the shadowgraphy method over the field-of-view lets one assign the motor position to the vacuum focus position.

$v_{th} = 1756 \frac{\mathrm{m}}{\mathrm{s}} = 1.756 \cdot 10^{-3} \frac{\mu\mathrm{m}}{\mathrm{ps}}$. The thermal expansion is then on the order of $0.5\,\mu$m and as the pixel size of the camera is only $0.51\,\mu$m this is not observable. Note, that the time scale of the expansion of electrons is shorter than for the considered hydrogen atoms.
Figure 5.10 shows the radius of the plasma channel for the different delays. The radius was defined as the $\exp(-2)$ value of the maximum electron density. The radius is constant within the error bars. The time scale of the plasma expansion is either smaller or larger than the time scale of the delay scan.

5.2.2 Plasma Generated by Hollow Beam

The energy was scanned from around 0.3 mJ to around 2.8 mJ. This was done by adding neutral density filters in front of the air compressor, in order to not change the temporal shape of the pulse after the compressor. For every filter setting 25 interferometer images were taken. A reference image of the imaging beam without a plasma signal was saved for the background subtraction in the analysis. The background from the ambient light was saved as well. The interferometer images were processed as described in section 4.2.2.
Figure 5.11 shows the averaged electron density at two energy settings. The top half shows the average electron density retrieved by the Abel transformation for an energy of 1.008 ± 0.175 mJ. The bottom half shows the density for an energy of 0.469 ± 0.143 mJ.

Unfortunately, no dip in electron density is visible on the axis at $r = 0\,\mu$m. From the simulation of the electron density with the intensity distribution of the focus scan, this result was already expected. At the lowest energy shot it was assumed, that a hollow channel could be observed. The intensity on the axis is at its lowest and thus the least probable to ionize the hydrogen. This was not the case, as the focal length of the plasma generating lens seems to be too short, therefore making the beam waist to narrow to observe the hollow structure. Several reasons are possible here. The resolution limit of the imaging system is $4.9 \pm 0.4\,\mu$m. If the simulation from the focus scan can be trusted, the inner channel radius is on the order of $3\,\mu$m. Therefore, the inner channel might not be resolvable. A second possible source for errors is the assumption of rotational symmetry, which is required for the Abel transformation. For the calculation the center of the plasma channel has to be chosen. At a pixel size of $0.510 \pm 0.039 \frac{\mu\mathrm{m}}{\mathrm{px}}$ being off by a few pixel while setting the center is a large source of error. While it can not be ruled out that a hollow plasma channel was created, it was not possible to detect it in this setting. Before starting the experiment the lowest energy was set

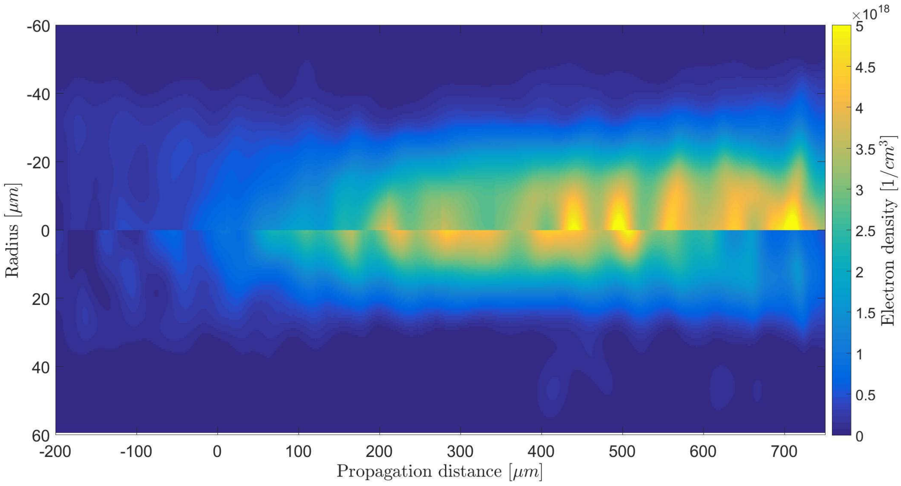

Figure 5.11: Comparison of two electron densities at different energies. Both plasma channel were created with the hollow laser beam propagating from right to left.

as that energy, where no signal could be seen on the interferometer camera by eye anymore. In retrospect, images should have been taken at lower energies and checked if an electron density is visible after the data processing.

The evolution of the channel radius during the energy scan is shown in figure 5.12. Every row represents a different measured plasma signal at a different energy. The radius was determined at the position where the electron density is $2.5 \cdot 10^{18}\,1/\mathrm{cm}^3$, which is half of the maximal density obtainable from 200 mbar hydrogen. As expected the radius increase with higher energies. Starting with a maximum radius of $3.12 \pm 0.31\,\mu$m at an energy of $0.323 \pm 0.048\,$mJ, the radius increases to $16.4 \pm 1.5\,\mu$m at an energy of $2.763 \pm 0.249\,$mJ. As the energy increases the beginning of the plasma is shifted more and more upstream. The intensity of the laser beam is sufficient to create a plasma earlier during its propagation at increasing energies. From the simulations of the short focal range we expect a more or less symmetric expansion of the plasma in both propagation directions from $z = 0$. In the radius figure 5.12 we notice that the plasma ends at roughly the same propagation distance at all energies. This is not explainable with the energy loss by ionizing the hydrogen alone. At least a second effect acts on the laser pulse. This could be plasma defocusing (see 2.2.4), an effect diffracting the laser pulse while propagating through a plasma with a radial gradient.

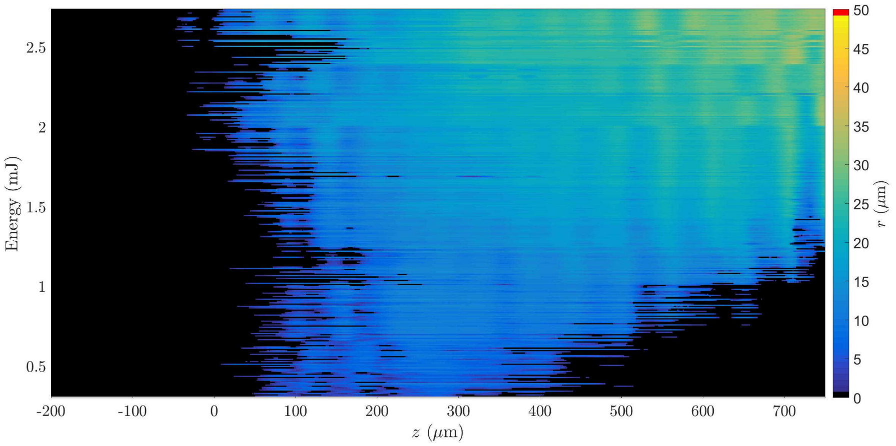

Figure 5.12: The figure shows the radius of the plasma channel at every propagation step for every energy shot of the hollow laser pulse.

5.2.3 Plasma Generated by Unmodified Beam

A second scan of the energy was done without the spiral phase plate inserted into the beam path. The plasma generated from this different laser profile should be distinguishable from the one described above. From the shape of the pulse depicted in figure 5.6 a plasma channel with lower radius and a higher electron density is expected for the same input energy. If this is visible conclusions can be made about the radial shapes of the plasma.

In figure 5.13 the electron density for both beam cases is compared at a similar energy of $0.44 \pm 0.14\,\mathrm{mJ}$ for the normal (top) and $0.47 \pm 0.14\,\mathrm{mJ}$ for the hollow beam (bottom). Again the averaged electron densities are plotted, where the laser beam is propagating from right to left. A full comparison of the generated plasma is not possible, as the first parts of the plasma were outside the field-of-view of the camera. But nevertheless, it is visible, that both channels have a comparable length. The laser intensity seems to be too low to ionize before even reaching the vacuum focus of the laser at the propagation distance $z = 0$. Again, this can not be explained by energy loss due to ionization alone but has to be related to ionization defocusing.

5.2.4 Location of First Plasma Formation

As the hollow character of the plasma channel was not observable at the vacuum focus position of the laser beam, the plasma generating lens was moved downstream, in order to image the beginning of the plasma. Due to

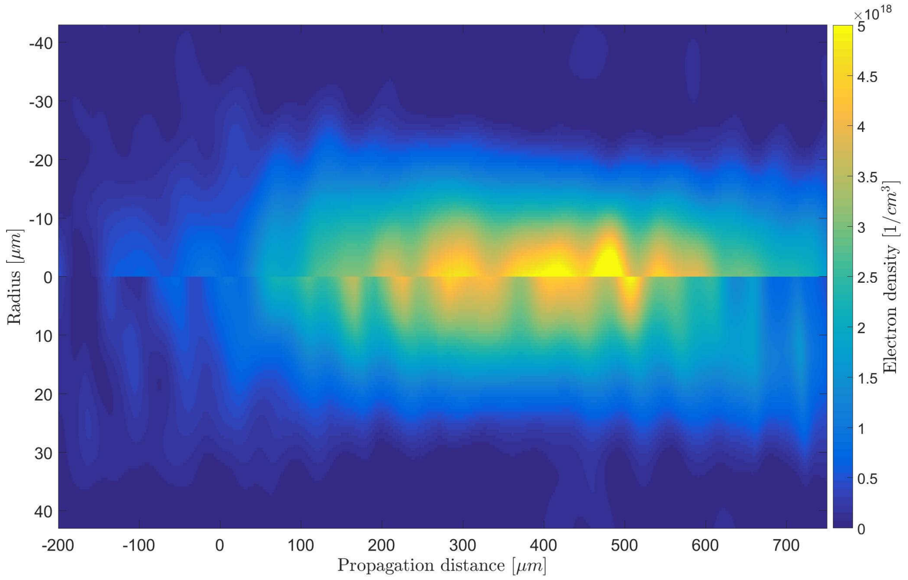

Figure 5.13: Comparison of two electron densities at the same energy, but for different generating beam geometries.

the short focal length a shift of around 1 mm of the lens increases the radius of the hollow laser beam by at least a factor of 2. At the beginning of the plasma the hollow shape should be well observable. The intensity off-axis is higher than on axis, so once the intensity off axis is high enough to ionize the hydrogen, the hollow shape should appear.

Figure 5.14 shows the electron density with the shifted lens position. The top half shows the plasma generated by the unmodified beam with $1.46 \pm 0.20\,\mathrm{mJ}$, while the bottom half shows the electron density generated by the hollow beam with $1.40 \pm 0.19\,\mathrm{mJ}$. At this position of the lens, imaging the start of the plasma channel, a clear difference between the two beam modes is visible. The beam created by the hollow laser beam has higher electron density off axis than on axis. This is a strong indicator that a hollow channel was created, at least at the start of the plasma channel. Later, during the propagation of the laser, the on-axis intensity is high enough to ionize the hydrogen as well and the hollow character is lost in our observation. On the other hand, the electron density of the channel created by the Gauss beam, also has electron density off axis between $z = 150\,\mu$m and $z = 500\,\mu$m. When looking at the laser profile 1 mm in front of the focus (figure 5.15) one notices, that the laser

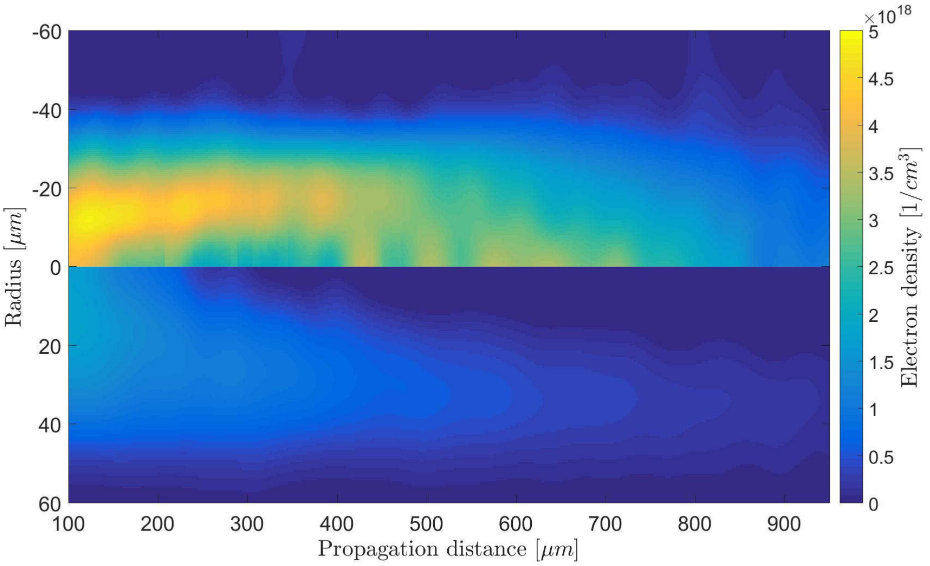

Figure 5.14: Comparison of the plasma channel created by the unmodified laser beam (top) and the hollow laser beam (bottom). The laser propagates from right to left.

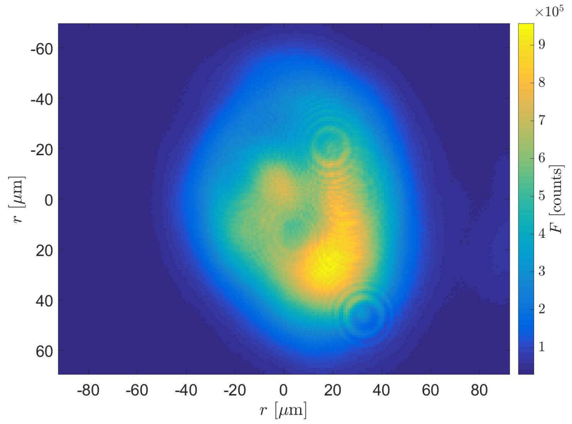

Figure 5.15: Laser profile for the unmodified beam 1 mm in front of the focus.

beam has almost a ring-like profile even without the phase plate. It is not entirely clear where this structure is coming from, but it seems that the off-axis electron density peak is caused by this laser intensity distribution.

Figure 5.16 shows the radial evolution of the electron density for

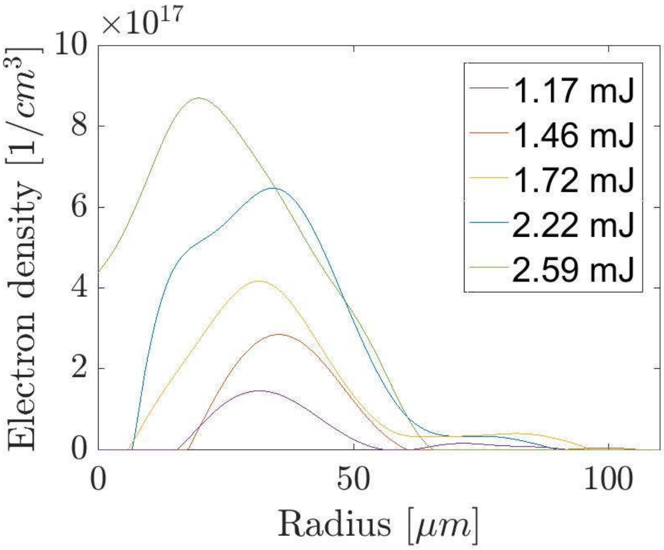

Figure 5.16: Electron density lineout for every measured energy at the beginning of the plasma.

increasing energies generated by the hollow beam. A lineout was taken at the same position $z = 765\mu$m for every measured energy. Even though the electron density is far from full ionization a general trend is visible. An inner channel can be observed for all five energies. With increasing energy, the inner channel gets narrower and the total extend of the plasma gets wider.

Figure 5.17 shows an overview of all measured plasma channels, where the laser propagates from right to left. For every propagation step at every shot the radius of the plasma channel is plotted. The radius was determined at the position where the electron density is $2.5 \cdot 10^{18}\,1/\mathrm{cm}^3$. The top left figure shows the plasma channels created by the hollow beam at the initial plasma generating lens position (compare section 5.2.2). The top right plot shows the plasma channel created with the hollow beam with the shifted lens position. The bottom plots show the plasma channel created by the unmodified beam at the same lens positions. The expansion of the plasma with higher energies can be observed from this orientation of the four plots. With higher energies the plasma expands asymmetrically in both directions. More plasma is generated earlier during the propagation of the laser. This is the same effect as explained earlier. With a higher laser intensity the plasma can be generated at an earlier position.

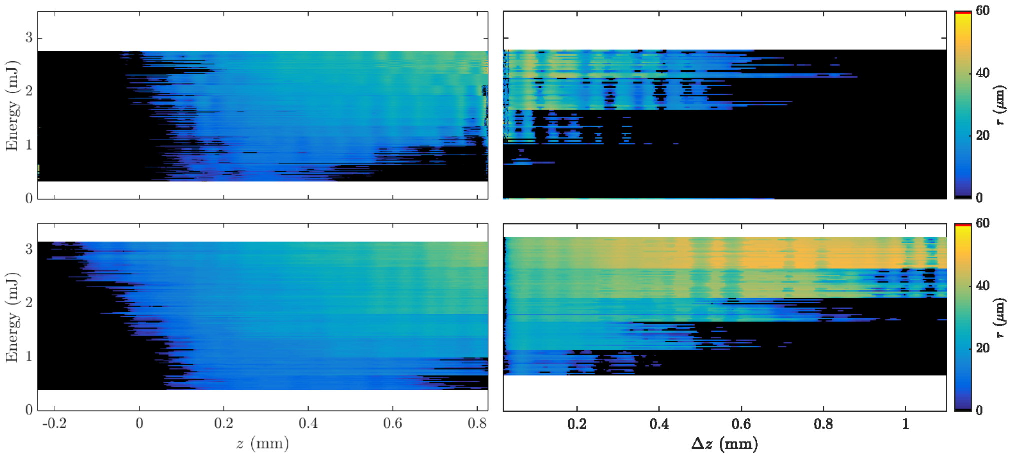

Figure 5.17: Radius of all measured plasma channels, where each plot shows a different setting. The top plots show the plasma generated by the hollow beam. The bottom plots show the plasma generated by the unmodified beam. The left plots show the plasma generated at the initial position of the plasma generating lens and the right plots show it for the position where the lens was shifted upstream.

5.3 Ionization Test Chamber Experiment

FLASHForward uses the laser system to create plasma, in which an electron bunch from the FLASH linear accelerator can drive wakefields to accelerate a trailing electron beam. The laser can be sent into a test laboratory, where a dedicated setup investigates the plasma creation process (see figure 5.18). A second setup accelerates electrons in an LWFA setup to explore electron beam diagnostics. The test setup uses a lens pair with a focal length of 18 m. This distance matches the focusing distance in the actual FLASHForward setup. In the following, the challenges of the plasma measurement in the ionization test chamber (ITC) are lined out and recommendations for future experiments are given.

During plasma-creation-experiments, it turned out that the lens pair in the test beamline introduced a significant B-integral effect on the beam. As a consequence, the actual FLASHForward laser beamline switched the focusing optics to two reflective concave mirrors. The focusing section in the test beamline towards the ITC could not be changed as of now since the laser supplies the LWFA experiment in the test laboratory as well.

However, the main challenge of the experiment at the ITC was, that the chamber is located in a radiation safe laboratory, due to the LWFA experi-

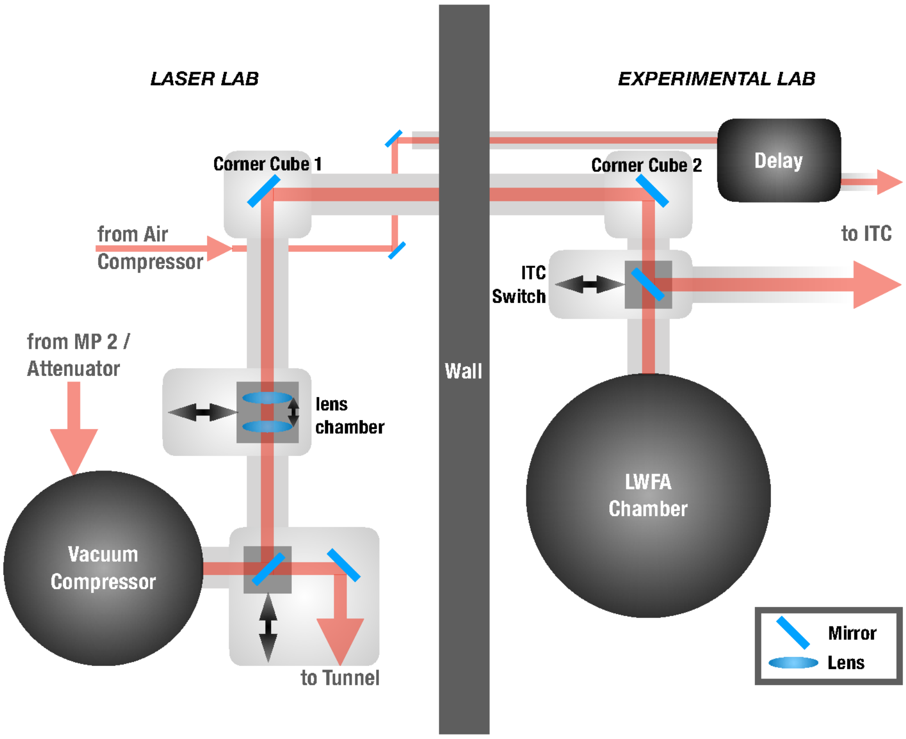

Figure 5.18: Overview of the beampath from the laser to the different experiments (by courtesy of Lars Goldberg).

ments. The laser can be propagated into the test lab in two energy modes. The so-called low-energy mode, where the laser is heavily attenuated in front of the vacuum compressor allows people to physically enter the room while the laser is present. Unfortunately, in this mode the laser does not have enough energy, mainly due to the weak focusing over 18 m, to ionize hydrogen in the ITC.

The second mode is the so called high-energy mode, where the laser can be operated at full power. When the high-power beam is propagating into the radiation laboratory the laser can reach intensities at which ionizing radiation is created. Therefore, the room must not be entered and is locked. A problem arises for the ionization experiments. The plasma interferometry (see figure 5.19) could not be set up while a plasma was present. The setup of such a diagnostic is not trivial when not being able to observe the plasma directly but using reference marks instead. In the end, the interferometer was not able to measure a plasma signal. Possible reasons could be a too small phase shift signal or the focal plane of the imaging system being not at the plasma position. Due to the safety regulations and a rather long procedure

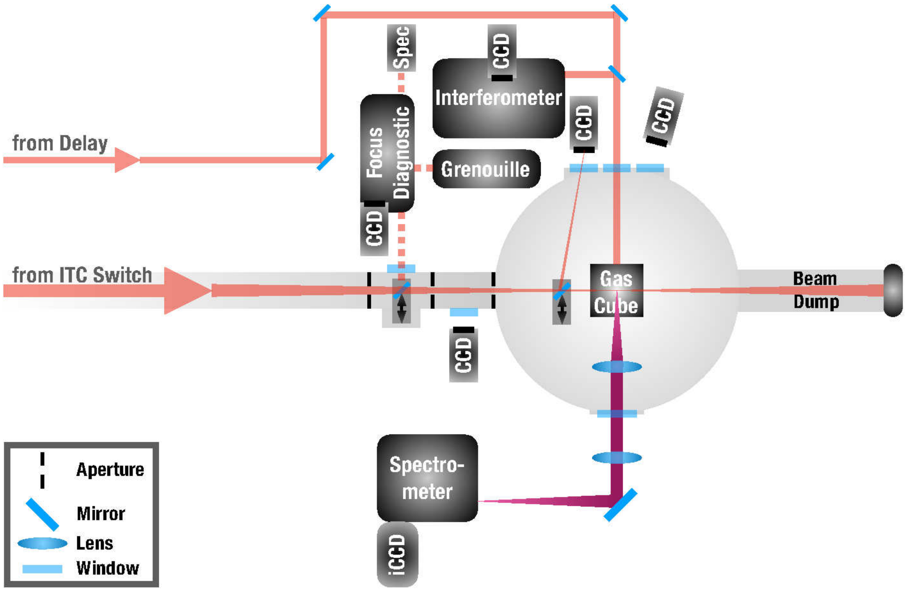

Figure 5.19: Illustration of the experimental setup at the ITC (by courtesy of Lars Goldberg).

from switching between low- and high-energy mode and as a result the realignment of the beam path, a second setup has been built to test the phase plate for this thesis.
Currently, the whole setup in the ITC is being redesigned with a higher degree of motorization and will be used to characterize the plasma target for FLASHForward in the first half of next year. Not only is it then possible to use interferometry for the observation of the plasma, but a spectroscopy setup is available for the detection of plasma light as well. First experiments on the spectrometer were already done and are currently being in the process of publishing[4].

---

[4] Lars Goldberg is currently writing his Ph.D. thesis on this subject and is about to finish in December 2017.

Chapter 6

Conclusion

6.1 Summery

In the present work, the generation of a hollow core plasma channel was studied. Several techniques were analyzed (section 3.1.1 and 3.1.2) and the most promising for the FLASHForward case was selected. With the use of a spiral phase plate (sec. 3.1.3) the laser pulse is transformed into a ring shape. The intensity distribution during the laser pulse propagation was simulated with the ray-tracing software Zemax in section 3.2. Using the obtained intensity maps the electron density was calculated varying the input parameters demonstrated that the topological charge of the phase plate has the biggest impact on the inner radius of the created hollow plasma channel. A higher charge will result in a larger radius. The laser energy can also vary the radius, but to a smaller degree as it just changes the area of the pulse in which ionization occurs.

An experiment was performed with a spiral phase plate with a topological charge of $l = 1$ with a testing setup, which had a different focusing geometry than used in FLASHForward. The laser pulse shape was measured during a focus scan (sec. 5.1), in which a ring shape was visible through the focal region. During the ionization experiment in hydrogen, the hollow shape could only be observed in a limited region (sec. 5.2). Only at the location of the first plasma formation and for energies above 0.9 mJ a hollow plasma channel was visible. The intensity of the laser pulse in the off-axis regions has to be high enough to ionize the hydrogen, while the inner part is not able to do so. This was only fulfilled in regions away from the vacuum focus spot of the laser. There are several reasons why the hollow character of the plasma could not be observed, including the resolution of the imaging system, the small focal length of the plasma generating lens, and the phase front of the laser pulse being not flat.

6.2 Outlook

The experimental work done in this thesis is far from optimal, as it is not resembling the plasma channel used in FLASHForward. The next step, of course, is testing of the hollow beam concept in the ionization test chamber with the correct focus geometry. Therefore, the ITC is currently redesigned. The focusing optics will be switched to the same reflective mirror pair as planned for FLASHForward. This eliminates the B-integral effect limiting beam quality, which was introduced by the lenses. The interior of the ITC is mostly rebuilt. It will feature the ability to move the imaging path and thus scan the plasma longitudinally. This way the z-axis can be calibrated to the vacuum focus position without shifting the plasma. The whole setup will be better motorized in order to control the plasma imaging from outside the test laboratory.

After the setup of the new ITC is done, the gas targets for FLASHForward can be characterized. Uniform plasma will be the first priority, but the hollow core plasma generated with the use of a spiral phase plate will soon follow. In these experiments, the already available SPP with the topological charge of $l = 1$ can be used. Later, higher charges can be used to generate plasmas with a larger inner radius. The plasma geometries will then be tested at different laser energies and varying gas pressures to get a good understanding of the plasma channel generated in the FLASHForward gas target.

The improvement of the laser phase can help to increase the focal spot quality of the laser beam. In the simulations done in chapter 3.2 the phase front could significantly alter the far-field intensity distribution. An adaptive optic such as a deformable mirror can change the phase front to the desired phase, in this case, a flat phase front.

It would also be interesting to do particle-in-cell simulations of the acceleration of electrons with the hollow plasma channel. This simulation could be done either from an electron density calculated from the intensity distribution in Zemax or a measured focus scan as a fully or semi theoretical approach, or with the electron densities obtained from the interferometry measurements. These results could then be compared with experimental data from FLASHForward, resulting in better simulation results or improvement in the plasma generating mechanisms.

Bibliography

[1] ATLAS Collaboration, "Observation of a new particle in the search for the Standard Model Higgs boson with the ATLAS detector at the LHC," *Physics Letters B*, vol. 716, no. 1, pp. 1–29, 2012.

[2] E. Esarey, C. B. Schroeder, and W. P. Leemans, "Physics of laser-driven plasma-based electron accelerators," *Reviews of Modern Physics*, vol. 81, no. 3, pp. 1229–1285, 2009.

[3] T. Tajima and J. M. Dawson, "Laser electron accelerator," *Physical Review Letters*, vol. 43, no. 4, pp. 267–270, 1979.

[4] J. Faure, Y. Glinec, A. Pukhov, S. Klselev, S. Gordienko, E. Lefebvre, J. P. Rousseau, F. Burgy, and V. Malka, "A laser-plasma accelerator producing monoenergetic electron beams," *Nature*, vol. 431, no. 7008, pp. 541–544, 2004.

[5] S. P. D. Mangles, C. D. Murphy, Z. Najmudin, A. G. R. Thomas, J. L. Collier, A. E. Dangor, E. J. Divall, P. S. Foster, J. G. Gallacher, C. J. Hooker, D. A. Jaroszynski, A. J. Langley, W. B. Mori, P. A. Norreys, F. S. Tsung, R. Viskup, B. R. Walton, and K. Krushelnick, "Monoenergetic beams of relativistic electrons from intense laser-plasma interactions," *Nature*, vol. 431, no. 7008, pp. 535–538, 2004.

[6] I. Blumenfeld, C. E. Clayton, F. J. Decker, M. J. Hogan, C. Huang, R. Ischebeck, R. Iverson, C. Joshi, T. Katsouleas, N. Kirby, W. Lu, K. A. Marsh, W. B. Mori, P. Muggli, E. Oz, R. H. Siemann, D. Walz, and M. Zhou, "Energy doubling of 42 GeV electrons in a metre-scale plasma wakefield accelerator," *Nature*, vol. 445, no. 7129, pp. 741–744, 2007.

[7] A. Aschikhin, C. Behrens, S. Bohlen, J. Dale, N. Delbos, L. Di Lucchio, E. Elsen, J. H. Erbe, M. Felber, B. Foster, L. Goldberg, J. Grebenyuk, J. N. Gruse, B. Hidding, Z. Hu, S. Karstensen,

A. Knetsch, O. Kononenko, V. Libov, K. Ludwig, A. R. Maier, A. Martinez De La Ossa, T. Mehrling, C. A. Palmer, F. Pannek, L. Schaper, H. Schlarb, B. Schmidt, S. Schreiber, J. P. Schwinkendorf, H. Steel, M. Streeter, G. Tauscher, V. Wacker, S. Weichert, S. Wunderlich, J. Zemella, and J. Osterhoff, "The FLASHForward facility at DESY," *Nuclear Instruments and Methods in Physics Research, Section A: Accelerators, Spectrometers, Detectors and Associated Equipment*, vol. 806, pp. 175–183, 2016.

[8] S. Gessner, *Demonstration of the Hollow Channel Plasma Wakefield Accelerator.* Dissertation, Stanford University, 2016.

[9] K. V. Lotov, "Acceleration of positrons by electron beam-driven wakefields in a plasma," *Physics of Plasmas*, vol. 14, no. 2, 2007.

[10] O. Svelto, *Principles of lasers.* 2010.

[11] C. Brabetz, *Development of specially shaped laser beams for the optimized acceleration of particles.* Dissertation, Johann Wolfgang Goethe-Universität Frankfurt, 2015.

[12] L. Allen, M. W. Beijersbergen, R. J. Spreeuw, and J. P. Woerdman, "Orbital angular momentum of light and the transformation of Laguerre-Gaussian laser modes," *Physical Review A*, vol. 45, no. 11, pp. 8185–8189, 1992.

[13] B. J., A., *Fundamentals of Plasma Physics Third Edition*, vol. 49. 2004.

[14] W. P. Leemans, C. E. Clayton, W. B. Mori, K. A. Marsh, P. K. Kaw, A. Dyson, C. Joshi, and J. M. Wallace, "Experiments and simulations of tunnel-ionized plasmas," *Physical Review A*, 1992.

[15] L. V. Keldysh, "Ionization in the field of a strong electromagnetic wave," *Soviet Physics JETP*, vol. 20, no. 5, pp. 1307–1314, 1965.

[16] M. V. Ammosov, N. B. Delone, and V. P. Krainov, "Tunnel ionization of complex atoms and of atomic ions in an alternating electromagnetic field," *Sov. Phys. JETP*, vol. 64, no. December 1986, pp. 1191–1194, 1986.

[17] J. Osterhoff, "Stable, ultra-relativistic electron beams by laser-wakefield acceleration." Januar 2009.

[18] G. Tauscher, *Ionisation of Hydrogen for Plasma Wakefield Accelerators.* Masterthesis, University Hamburg, 2016.

[19] C. B. Schroeder, E. Esarey, C. Benedetti, and W. P. Leemans, “Control of focusing forces and emittances in plasma-based accelerators using near-hollow plasma channels,” *Physics of Plasmas*, vol. 20, no. 8, p. 080701, 2013.

[20] C. Schroeder, D. Whittum, and J. Wurtele, “Multimode Analysis of the Hollow Plasma Channel Wakefield Accelerator,” *Physical Review Letters*, vol. 82, no. 6, pp. 1177–1180, 1999.

[21] S. Gessner, E. Adli, J. M. Allen, W. An, C. I. Clarke, C. E. Clayton, S. Corde, J. P. Delahaye, J. Frederico, S. Z. Green, C. Hast, M. J. Hogan, C. Joshi, C. A. Lindstrøm, N. Lipkowitz, M. Litos, W. Lu, K. A. Marsh, W. B. Mori, B. O’Shea, N. Vafaei-Najafabadi, D. Walz, V. Yakimenko, and G. Yocky, “Demonstration of a positron beam-driven hollow channel plasma wakefield accelerator,” *Nature Communications*, vol. 7, p. 11785, 2016.

[22] “Sasada Lab website - Research.”

[23] M. W. Beijersbergen, L. Allen, H. E. van der Veen, and J. P. Woerdman, “Astigmatic laser mode converters and transfer of orbital angular momentum,” *Optics Communications*, vol. 96, no. 1-3, pp. 123–132, 1993.

[24] M. Padgett, J. Arlt, N. Simpson, and L. Allen, “An Experiment To Observe The Intensity And Phase Structure Of Laguerre-Gaussian Laser Modes,” *Am. J. Phys.*, vol. 64, no. 1, pp. 77–82, 1996.

[25] A. Mawardi, “Generation of a donut beam for a tight radial confinement of atoms in a one-dimensional optical lattice,” 2010.

[26] R. Oron, N. Davidson, A. a. Friesem, and E. Hasman, “Efficient formation of pure helical laser beams,” *Optics Communications*, vol. 182, no. 1-3, pp. 205–208, 2000.

[27] J. Durnin, “Exact solutions for nondiffracting beams I The scalar theory,” *Journal of the Optical Society of America A*, vol. 4, no. 4, p. 651, 1987.

[28] J. Fan, E. Parra, I. Alexeev, K. Kim, H. Milchberg, L. Margolin, and L. Pyatnitskii, “Tubular plasma generation with a high-power hollow bessel beam,” *Physical review. E, Statistical physics, plasmas, fluids, and related interdisciplinary topics*, vol. 62, no. 6 Pt A, pp. R7603–6, 2000.

[29] D. Mcgloin and K. Dholakia, “Bessel beams: Diffraction in a new light,” *Contemporary Physics*, vol. 46, no. 1, pp. 15–28, 2005.

[30] N. E. Andreev, S. S. Bychkov, V. V. Kotlyar, L. Y. Margolin, L. N. Pyatnitskii, and P. G. Serafimovich, “Formation of high-power hollow Bessel light beams,” *Quantum Electronics*, vol. 26, no. 2, pp. 126–130, 1996.

[31] M. W. Beijersbergen, R. P. Coerwinkel, M. Kristensen, and J. P. Woerdman, “Helical-wavefront laser beams produced with a spiral phaseplate,” *Optics Communications*, vol. 112, no. 5-6, pp. 321–327, 1994.

[32] R. Trebino, P. O’Shea, M. Kimmel, and X. Gu, “Measuring Ultrashort Laser Pulses Just Got a Lot Easier,” *Optics and Photonics News*, vol. 12, no. 6, p. 22, 2001.

[33] R. Trebino, *Frequency-Resolved Optical Gating: The Measurement of Ultrashort Laser Pulses.* Springer, 2000.

[34] X. Michalet and S. Weiss, “Using photon statistics to boost microscopy resolution.,” *Proceedings of the National Academy of Sciences of the United States of America*, vol. 103, no. 13, pp. 4797–4798, 2006.

[35] M. Takeda, H. Ina, and S. Kobayashi, “Fourier-transform method of fringe-pattern analysis for computer-based topography and interferometry,” *Journal of the Optical Society of America*, vol. 72, no. 1, p. 156, 1982.

[36] C. Lukas, M. Muller, V. S.-v. D. Gathen, and H. F. Dobele, “Spatially Resolved Electron Density Distribuition in an RF Excited Parallel Plate Plasma Reactor by 1 mm Microwave Interferoetry,” *Plasma Sources Sci Technol*, vol. 8, pp. 94–99, 1999.

[37] M. Rosete-Aguilar, F. C. Estrada-Silva, N. C. Bruce, C. J. Román-Moreno, and R. Ortega-Martínez, “Calculation of temporal spreading of ultrashort pulses propagating through optical glasses,” *Revista Mexicana de Fisica*, vol. 54, no. 2, pp. 141–148, 2008.

[38] W. Welford, *Aberrations of Optical Systems.* New York: Taylor & Francis Group, 1986.

Declaration

I hereby confirm that I have authored this Master's thesis independently and without use of others than the indicated sources. All passages which are literally or in general matter taken out of publications or other sources are marked as such. The printed version matches the one on the electronic storage device.

Hamburg, December 2, 2017

Heinrich Martin Quast